Monthly Notices of the ROYAL ASTRONOMICAL SOCIETY

MNRAS **537,** 2024–2045 (2025) https://doi.org/10.1093/mnras/staf116
Advance Access publication 2025 January 21

A systematically selected sample of luminous, long-duration, ambiguous nuclear transients

P. Wiseman [1]★ R. D. Williams,[2] I. Arcavi,[3] L. Galbany,[4,5] M. J. Graham [6] S. Hönig,[1] M. Newsome,[7,8] B. Subrayan,[9] M. Sullivan [1] Y. Wang [10] D. Ilić [11,12] M. Nicholl [13] S. Oates [14] T. Petrushevska[15] and K. W. Smith[13]

[1]*School of Physics and Astronomy, University of Southampton, Southampton SO17 1BJ, UK*
[2]*Royal Observatory, University of Edinburgh, Edinburgh EH9 3HJ, UK*
[3]*The School of Physics and Astronomy, Tel Aviv University, Tel Aviv 69978, Israel*
[4]*Institute of Space Sciences (ICE-CSIC), Campus UAB, Carrer de Can Magrans, s/n, E-08193 Barcelona, Spain*
[5]*Institut d'Estudis Espacials de Catalunya (IEEC), E-08860 Castelldefels (Barcelona), Spain*
[6]*California Institute of Technology, 1200 E. California Boulevard, Pasadena, CA 91125, USA*
[7]*Las Cumbres Observatory, 6740 Cortona Drive, Suite 102, Goleta, CA 93117-5575, USA*
[8]*Department of Physics, University of California, Santa Barbara, CA 93106-9530, USA*
[9]*Department of Physics and Astronomy, Purdue University, 525 Northwestern Avenue, West Lafayette, IN 47907, USA*
[10]*Key Laboratory of Optical Astronomy, National Astronomical Observatories, Chinese Academy of Sciences, Beijing 100101, China*
[11]*Department of Astronomy, Faculty of Mathematics,University of Belgrade, Studentski trg 16, 11000 Belgrade, Serbia*
[12]*Hamburger Sternwarte, Universitat Hamburg, Gojenbergsweg 112, D-21029 Hamburg, Germany*
[13]*Astrophysics Research Centre, School of Mathematics and Physics, Queen's University Belfast, Belfast BT7 1NN, UK*
[14]*Physics Department, Lancaster University, Bailrigg, Lancaster LA1 4YB, UK*
[15]*Center for Astrophysics and Cosmology, University of Nova Gorica, Vipavska 11c, SI-5270 Ajdovščina, Slovenia*

Accepted 2025 January 9. Received 2025 January 9; in original form 2024 June 17

ABSTRACT

We present a search for luminous long-duration ambiguous nuclear transients (ANTs) similar to the unprecedented discovery of the extreme ambiguous event AT2021lwx with a > 150 d rise time and luminosity $10^{45.7}$ erg s^{-1}. We use the Lasair transient broker to search Zwicky Transient Facility (ZTF) data for transients lasting more than one year and exhibiting smooth declines. Our search returns 59 events, 7 of which we classify as ANTs assumed to be driven by accretion onto supermassive black holes. We propose the remaining 52 are stochastic variability from regular supermassive black hole accretion rather than distinct transients. We supplement the seven ANTs with three nuclear transients in ZTF that fail the light curve selection but have clear single flares and spectra that do not resemble typical active galactic nucleus. All of these 11 ANTs have a mid-infrared flare from an assumed dust echo, implying the ubiquity of dust around the black holes giving rise to ANTs. No events are more luminous than AT2021lwx, but one (ZTF19aamrjar) has twice the duration and a higher integrated energy release. On the other extreme, ZTF20abodaps reaches a luminosity close to AT2021lwx with a rise time < 20 d and that fades smoothly in > 600 d. We define a portion of rise-time versus flare amplitude space that selects ANTs with ~ 50 per cent purity against variable AGNs. We calculate a volumetric rate of $\gtrsim 3 \times 10^{-11}$ Mpc^{-1} yr^{-1}, consistent with the events being caused by tidal disruptions of intermediate and high-mass stars.

Key words: accretion, accretion discs – galaxies: active – transients: tidal disruption events.

1 INTRODUCTION

Untargeted large-area photometric surveys have led to the identification of several intriguing classes of astrophysical transients whose characteristic time-scales lie outside the weeks-to-month duration occupied by conventional supernovae. The optical transient parameter space now extends to fast, luminous, blue optical transients (FBOTs; e.g. Drout et al. 2014; Pursiainen et al. 2018; Wiseman et al. 2020; Ho et al. 2023) and slowly evolving superluminous supernovae (SLSNe; e.g. Quimby et al. 2011; Nicholl et al. 2017; Inserra et al. 2018; Angus et al. 2019; Chen et al. 2023). The destruction of stars by black holes – tidal disruption events (TDEs; Hills 1975; Rees 1988) – have also entered the era of sample studies (Arcavi et al. 2014; Leloudas et al. 2019; Gezari 2021; van Velzen et al. 2021; Charalampopoulos et al. 2022; Nicholl et al. 2022; Hammerstein et al. 2023; Yao et al. 2023a). One of the most extreme and energetic transient phenomena of all, however, are still restricted to a handful of heterogeneously selected events whose discoveries have been serendipitous, whose observational classification is uncertain, and whose physical origin is unknown. So-called ambiguous nuclear transients (ANTs; e.g. Kankare et al. 2017; the most luminous of which have been named

★ E-mail: P.S.Wiseman@soton.ac.uk

extreme nuclear transients, ENTs; Hinkle et al. 2024) appear to be related to supermassive black holes (SMBHs), their observational properties straddling the boundaries between single-star TDEs and continuously accreting active galactic nuclei (AGNs). ANTs are loosely defined as nuclear transients (i.e. those spatially coincident with the nuclei of galaxies) whose combination of light curves and spectra do not fit any of the TDE, AGN, or SN classes. They typically are characterized by long-lived, luminous optical flares with smooth rises and power-law decays (Graham et al. 2017).

AGN are inherently variable across the entire electromagnetic spectrum: in the ultraviolet–optical–near-infrared (UVOIR), the variability is stochastic on time-scales from seconds to years, and is typically limited to amplitudes $\lesssim 0.5$ mag on these time-scales (e.g. Vanden Berk et al. 2004; MacLeod et al. 2010; Caplar, Lilly & Trakhtenbrot 2017; Sheng, Ross & Nicholl 2022). Their variations are often described by a stochastic process called a damped random walk (DRW; Kelly, Bechtold & Siemiginowska 2009). The presence of short-term variability in the optical is challenging to the canonical thin viscous accretion disc model (e.g. Antonucci 2018; Lawrence 2018) and indicates that the disc reprocesses higher frequency (i.e. X-ray) emission from a small central region (e.g. Clavel et al. 1992; McHardy et al. 2016). Such reprocessing, however, fails to explain the increasing number of AGN showing large-amplitude changes on short time-scales: it is estimated that up to 30–50 per cent of quasars show variability at the ~ 1 mag level over baselines of 15 yr (Rumbaugh et al. 2018), dubbed 'extreme variability quasars' (EVQs). Another growing class of AGN is that showing distinct spectral changes on years – decade time-scales: the (dis)appearance of broad emission lines (e.g. LaMassa et al. 2015; MacLeod et al. 2016), sometimes temporally coincident with a change in flux. So-called changing-look AGN (CLAGNs) challenge theories of AGN emission mechanisms even more (for a review, see Ricci & Trakhtenbrot 2023). Correlations between the continuum luminosity and broad emission line appearance indicate that changes in the accretion flow drive CLAGNs, also called changing *state* AGNs.[1] In one extreme case, a non-variable AGN appears to 'switch on' its variability over the course of a few years (Ridley et al. 2024) while another changes its spectral state on a timescale of months (Trakhtenbrot et al. 2019b).

The distinction between ANTs and AGN flares, CLAGNs, and TDEs is not clearly defined. Indeed, TDEs are not excluded from occurring in AGN. ANT light curves appear to fall into two categories. Some ANT light curves are very smoothly evolving, rising slowly and decline monotonically even slower, including AT2019brs (Frederick et al. 2021), Gaia16aaw/AT2016dbs and Gaia18cdj/AT2018fbb (Hinkle et al. 2024), and the most energetic transient ever discovered, AT2021lwx (Subrayan et al. 2023; Wiseman et al. 2023). This behaviour appears to be a slower version of the evolution of most TDEs. Other ANTs, although displaying a single overall flare, show variability superimposed over their long-term light curves, such as AT2019fdr (Frederick et al. 2021; Pitik et al. 2022; Reusch et al. 2022), ASASSN-15lh (Leloudas et al. 2016)[2], ASASSN-17jz (Holoien et al. 2022), ASASSN-18jd (Neustadt et al. 2020), PS16dtm (e.g. Blanchard et al. 2017; Petrushevska et al. 2023), AT2017bgt (Trakhtenbrot et al. 2019a), and Swift J2219510−484240 (Oates et al. 2024). While their light curves are similar to TDEs, ANTs are spectroscopically more similar to AGN with high equivalent width emission lines (particularly from the hydrogen Balmer series), while TDE emission lines are much broader but weaker. A subset of ANTs show features associated with Bowen fluorescence such as He II and N III, indicative of a steep far-UV or soft X-ray source such as accretion disc, and are termed Bowen fluorescence flares (BFFs; Trakhtenbrot et al. 2019a). Some events classified as TDEs also have signatures of Bowen fluorescence, complicating the distinction between TDEs and ANTs further but hinting that the emission mechanisms are similar, irrespective of the source of accretion (Blagorodnova et al. 2017; Leloudas et al. 2019; Velzen et al. 2021). Frederick et al. (2021) presented a small sample of ANTs in known narrow-line Seyfert 1 (NLSy1) AGN, a class of Seyfert galaxies accreting close to the Eddington limit. PS16dtm also occurred in a NLSy1 (Blanchard et al. 2017), while PS1-10adi also showed similar features (Kankare et al. 2017), raising the possibility that ANTs preferentially occur in such systems.

An extra piece of the TDE–ANT–AGN puzzle is provided by mid-infrared (MIR) observations that probe hot dust. MIR flares, which tend to lag the UVOIR, accompany many of the UVOIR-discovered ANTs (Petrushevska et al. 2023; Wiseman et al. 2023; Hinkle 2024; Oates et al. 2024), as well as existing alone without optical counterparts (Jiang et al. 2021a; Wang et al. 2022). MIR flares are observed less frequently in TDEs (Velzen et al. 2016), although the population of MIR flares without optical counterparts (Jiang et al. 2021a; Masterson et al. 2024) could be caused by fully obscured TDEs. The interpretation is that these MIR-loud ANTs occur in nuclei with circumnuclear dust, typically described as the AGN 'torus'. Nevertheless, some ANTs show no sign of previous AGN activity and optical spectra distinct from typical AGN (e.g. Oates et al. 2024).

The recent discovery of AT2021lwx as the most energetic transient ever discovered pushed the boundaries of our understanding of SMBH accretion (Subrayan et al. 2023; Wiseman et al. 2023). For the extreme luminosity (7×10^{45} erg s^{-1}) and duration (> 600 d in the rest frame), and thus total energy release ($> 10^{53}$ erg), to be explained by tidal disruption requires an unlikely combination of a large black hole mass ($10^{8.3}$ M$_\odot$) and a massive (15 M$_\odot$) star. Meanwhile, the lack of forbidden oxygen and of any pre-cursory activity or shorter term variability makes an AGN implausible. In this paper, we perform a systematic search for ANTs similar to AT2021lwx. We seek to understand whether it belongs to a population with similar energetics. We perform a census of nuclear transients with the aim of setting a standard distinction between ANTs and extreme but 'standard' variability of AGN.

In Section 2, we introduce the search for ANTs in the Zwicky Transient Facility (ZTF) data stream. In Section 3, we present the individual ANTs and their shared properties. In Section 4, we compare the variability properties of ANTs and AGN. We discuss the implications on the nature of ANTs in Section 5, and conclude in Section 6. Where relevant, we assume a spatially flat Lambda-cold dark matter (ΛCDM) cosmology with $H_0 = 70\,\mathrm{km\,s^{-1}\,Mpc^{-1}}$ and $\Omega_\mathrm{M} = 0.3$. Unless otherwise stated, uncertainties are presented at the $1\,\sigma$ level. Magnitudes are presented in the AB system (Oke & Gunn 1983).

2 SAMPLE SELECTION

We search for ANTs in the ZTF (Bellm et al. 2019; Graham et al. 2019). ZTF is a wide-field, high-cadence survey that is extremely effective at detecting supernovae at low ($z \lesssim 0.15$) redshift. Frederick

[1]Note that changing-look has also been used to describe those AGNs that change X-ray properties, which can also be denoted changing *obscuration* AGN (Ricci & Trakhtenbrot 2023).

[2]Interpreted in Leloudas et al. (2016) and Krühler et al. (2018) as a TDE, but by Dong et al. (2016) as a SLSN.

et al. (2021) presented five ANTs serendipitously identified within the first 2 yr of the ZTF survey. Of these, two (AT2019brs and AT2019fdr) are photometrically 'AT2021lwx-like' with single UV-optical flares lasting over 1 yr. The cadence, depth, and now nearly 6-yr baseline make ZTF the ideal survey to search for further ANTs. However, the selection of true nuclear transients compared to regular AGN variability or SNe is non-trivial (e.g. Dgany et al. 2023). In this section, we describe the methods used to retrieve transients and identify ANTs in ZTF data.

2.1 Filtering of slow, nuclear transients

To search for ANTs in the ZTF data, we use the LASAIR[3] transient broker (Smith et al. 2019) via its public application programming interface (API). The LASAIR API allows programmatic queries of the ZTF transient detection data base via a number of criteria. We outline our initial selection criteria below.

2.1.1 Nuclear transients

ANTs are, by definition, located in galaxy nuclei. To select nuclear transients, we use the SHERLOCK sky context software (Smith et al. 2020) running in LASAIR. The ZTF search area is fully covered by the Panoramic Survey Telescope and Rapid Response System (Pan-STARRS1) science consortium surveys (Chambers et al. 2016; Wainscoat et al. 2016): sherlock uses the Pan-STARRS catalogues and probabilistic classifications of unresolved point sources (Tachibana & Miller 2018) to determine a host galaxy and the transient location within that host. We select all objects that are predicted as Nuclear Transients (i.e. transients consistent with a galactic nucleus) or AGN (transients consistent with a galactic nucleus that are listed in an AGN catalogue). Note that most transient searches exclude known AGN, but we allow them to avoid excluding bona-fide transient events associated with actively accreting SMBHs. We also include all objects predicted as SNe (transients not entirely consistent with a galaxy nucleus) with an angular separation of < 0.4 arcsec from the catalogued centre of a galaxy, based on the requirements used for the ZTF TDE samples (Velzen et al. 2021; Yao et al. 2023a). We verify the nuclear origin of any transients in our sample by validating that their mean position lies within 0.3 arcsec of the catalogued galaxy position, roughly equivalent to the ZTF positional uncertainty. Finally, we include 'Orphan' transients, which have no associated host galaxy in deeper survey imaging (as was the case for AT2021lwx). Including transient that appear hostless prevents the systematic exclusion of events at high-redshift, extremely dusty, or uncatalogued dwarf galaxies.

2.1.2 Long-duration, high quality light curves

The LASAIR API does not contain a parameter representing the duration of a light curve, as the queryable data base only deals with 30-d alert packets[4] rather than entire light curves. To filter out short-duration transients or those with poor coverage, we require the alert packet to have more than 10 detections (across both bands) of good quality and brighter than the reference (referred to as `ncandgp>` 10).

[3]https://lasair-ztf.lsst.ac.uk/
[4]https://zwickytransientfacility.github.io/ztf-avro-alert/

Table 1. Sample selection for ZTF nuclear transient candidates.

Selection	Number cut	Number remaining
Initial selection	–	53 164
< 50 points	33 187	19 977
$t_{max} - t_{min} < 1$ yr	1439	18 538
$\Delta m < 1$	15 276	3262
Linear fit	9165	58
Visual inspection	51	7

Table 2. Sample selection for ZTF orphan transients.

Selection	Number cut	Number remaining
Initial selection	–	4529
< 50 points	3923	606
$t_{max} - t_{min} < 1$ yr	331	275
$\Delta m < 1$	268	7
Linear fit	6	1
Visual inspection	0	1

2.2 Photometric selection of ANTs

Roughly 50 000 nuclear transient candidates and ~ 4000 hostless transient candidates pass our initial queries. We retrieve difference image photometry light curves via the LASAIR API of these events and make several further selections in order to identify ANT candidates. The number of events passing this selection are described in Tables 1 and 2 for nuclear and hostless transients, respectively. This selection applies to the ZTF g and r bands separately: an event failing either band will fail the overall cut.

We are aware that each of the following criteria, in particular the visual inspection, may introduce biases because we do not know what ANTs are. We are insensitive to events in off-nuclear black holes, as well as events with strong rebrightenings or variability during the decline, and events that are still ongoing (not yet declining) or did not have any detections on the rise. The nominal selection instead is aimed at selecting a high-purity sample of events similar to AT2021lwx. We subsequently test three alternative selections to verify the completeness achieved by the nominal selection.

(i) Light curve coverage: we require good quality light curve coverage, so events with fewer than 50 detections in each of the g and r bands are rejected. This selection removes objects with short-duration flares or noisy episodes.

(ii) Duration: ANTs are long-lived transients and we require that the most recent detection in at least one filter must be at least 300 d after the first detection.

(iii) Amplitude: AGNs are naturally variable, but this variability is usually limited to a $\lesssim 0.5$ mag over long time-scales (e.g. MacLeod et al. 2010). To exclude most AGN variability, we require events to show a brightening of at least 1 mag during the ZTF observing period. We make this selection on the difference between the brightest and faintest detection in either band.

(iv) Single, smooth decline: Any remaining AGNs and variable stars should show stochastic variability on time-scales shorter than the typical decline of an ANT, a property we denote 'bumpiness'. We define the opposite, 'smoothness', as the lack of variability above the photometric noise on time-scales shorter than the main light curve. Single transient events show power-law or exponential decays, which are linear in magnitude space. We fit the declines with a linear

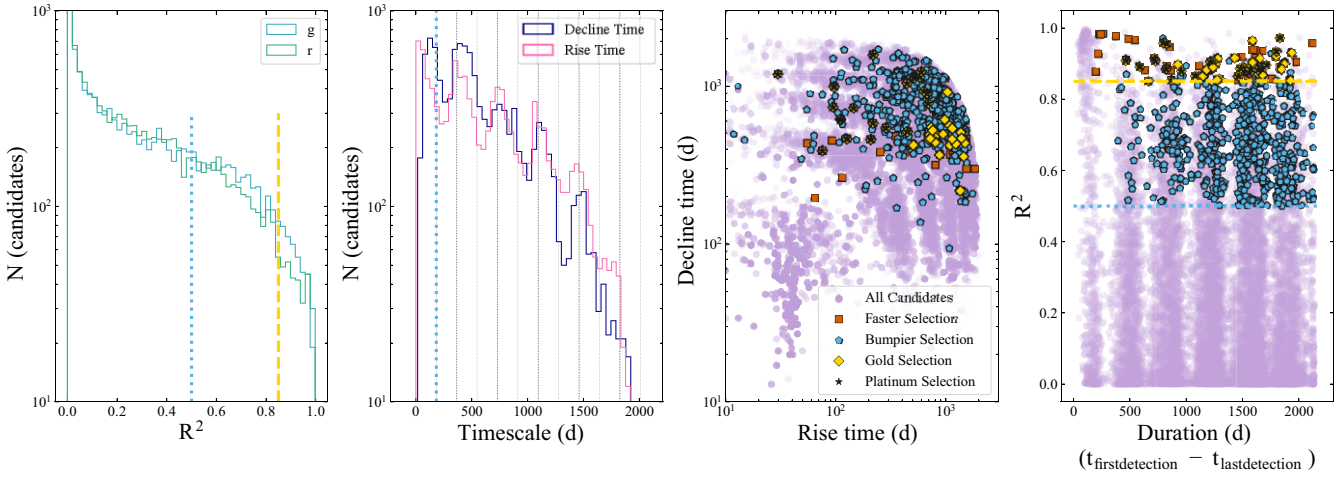

Figure 1. Light curve properties of nuclear transients in ZTF. In each panel the gold dashed and blue dotted lines indicate the threshold for the gold sample and bumpier samples, respectively. (a) Histogram of the Pearson R^2 for the linear fit to light curve declines in the g and r bands; (b) Histogram of the rise and decline time-scales to the brightest point in the r-band light curve. 300- and 0.5-yr intervals are marked with vertical lines; (c) r-band rise time versus decline time to/from the peak brightness; (d) Pearson R^2 versus total r-band duration.

model and quantify the goodness-of-fit to the linear model with the Pearson r^2 parameter. We set an arbitrary threshold of $r^2 > 0.85$ for a decline to be accepted as smooth and linear. We vary this definition of 'smoothness' below and determine its effect on the number of high-quality candidates to be minimal.

The distribution of candidates in these parameter spaces is shown in Fig. 1. After all the nominal selection criteria are applied, we are left with 58[5] and one orphan (ZTF20abrbeie = AT2021lwx), which we denote the 'gold selection'. Of the ANTs published by Frederick et al. (2021), we recover ZTF19aailpwl = AT2019brs (the other three are too 'bumpy'). To explore ANTs with different light curve shapes, we subsequently trial a set of different selection criteria, which are described in Appendix A. Briefly, we conduct a search for faster-declining events by relaxing the maximum duration to 180 d (the 'faster' sample), for less smooth events by relaxing the linear decline correlation coefficient to $R^2 > 0.5$ (the 'bumpier' sample), and the decline time to be longer than the rise time (the 'platinum' sample). The resulting samples and their ZTF light curve properties are available online[6]. For the 58 gold events, we obtain forced photometry for the full ZTF survey duration via the ZTF forced photometry service (Masci et al. 2019) for visual inspection.

2.2.1 *Visual inspection*

We visually inspect all 58 light curves and assign visual classifications of 'Transient', 'AGN', or 'Unclear' according to the flowchart in Fig. 2. These classifications are predominantly based on pre-and post-peak variability. In particular, the forced photometry allows us to view any variability that occurred before the candidate passed the alert threshold in ZTF. We classify 16 events as Transients, six as Unclear, and 36 as AGNs.

[5]59 separate candidate light curves passed, but we note that ZTF22aadesap and ZTF22aafuzjv are two identifiers for the same light curve, leaving 58 distinct transients. light curves of nuclear transients.
[6]https://github.com/wisemanp/ANTs-Nest

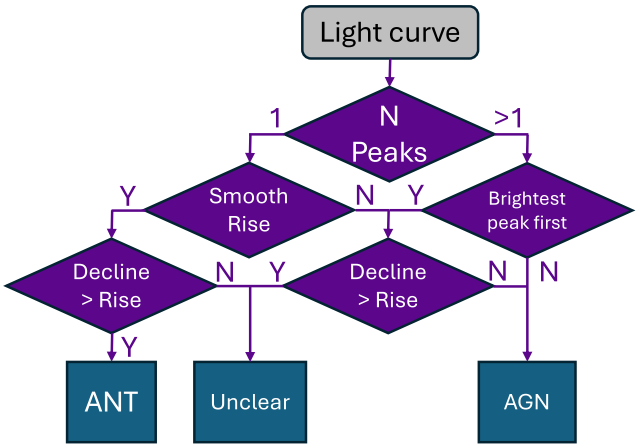

Figure 2. Flowchart used while visually inspecting the ANT candidates passing selection criteria. 'Y' refers to a light curve passing criteria, while N is for failing.

2.2.2 *Spectroscopic history and follow-up*

For the analysis in this paper, we require spectroscopy for two reasons: first, it is needed to remove non-ambiguous transients that were selected photometrically (i.e. supernovae and TDEs); and secondly, in order to estimate the absolute luminosity, energetics, and the elemental composition of ANTs. Of the 58 'gold' light curves, 18 were reported as transients to the Transient Name Server (TNS)[7], and a handful have been publicly spectroscopically classified. Note that ANT is not a spectroscopic classification. Here, we cross-match the candidates we photometrically classified as transients with the public classifications. In the cases where the spectra are clearly supernovae, we discard the events from our sample. We do not discard events with AGN-like spectra if the light curves are classified as Transient (these are, by definition, ANTs). We also check transients labelled as Unclear – if they have AGN-like spectra we discard them as long-time-scale AGN variability.

[7]https://www.wis-tns.org/

Table 3. Sample properties for the 11 events passing our selection criteria, split into smoothly evolving (upper) and spectroscopic (lower) selections.

ZTF ID	RA	Dec.	IAU name	Cross-matches	Host r-mag	Redshift
				Photometric ANTs		
ZTF20abrbeie	318.451 73	27.430 66	AT2021lwx	ATLAS20bkdj, PS22iin	No detected host	0.9945 [abc]
ZTF19aamrjar	272.339 63	25.309 19	–	ATLAS19mmu	18.3	0.697[d]
ZTF20abodaps	359.808 15	−17.696 58	AT2020afep	ATLAS20vrw	19.8	0.607[d]
ZTF18aczpgwm	33.790 96	7.164 53	AT2019kn	ATLAS19bdfo, Gaia19abv	19.1	0.4279[d]
ZTF21abxowzx	324.333 04	−10.753 312	AT2021yzu	ATLAS21bjoi	20.3	0.419[e]
ZTF19aailpwl	216.943 40	29.510 61	AT2019brs	ATLAS19fyh, Gaia19axp	19.3	0.3736[f]
ZTF20abgxlut	257.765 25	6.736 331	AT2020oio	Gaia20dvv, ATLAS20rmk	20.4	0.247[g]
ZTF20aadesap	232.765 45	53.405 35	AT2022fpx	ATLAS22kjn, Gaia22cwy, PS23bdt	17.9	0.073[h]
ZTF18acvvudh	117.708 4916	1.358 392 278	AT2018lcp		18.6	–
ZTF22aaaeons	231.827 862	−8.532 609	AT2022zg	Gaia22aft, ATLAS22ery	18.5	–
				Supplementary spectroscopic ANTs		
ZTF20acvfraq	349.724 03	−10.584 89	AT2020adpi	ATLAS20bjzp, Gaia21aid	19.7	0.26[i]
ZTF19aatubsj	257.278 57	26.855 69	AT2019fdr	ATLAS19lkd	18	0.2666[j,h]
ZTF20aanxcpf	15.165 08	39.708 42	AT2021loi	ATLAS21qje	18	0.083[k]

Note. [a]Grayling et al. (2022); [b]Subrayan et al. (2023); [c]Wiseman et al. (2023); [d]This work; [e]Chu, Dahiwale & Fremling (2021a); [f]Frederick et al. (2021); [g]Terreran et al. (2020); [h]Perez-Fournon et al. (2022); [i]Chu, Dahiwale & Fremling (2021b); [j]Chornock et al. (2019); [k]Makrygianni et al. (2023).

Of the 16 long-duration events we classified as transients via visual inspection, five are spectroscopically classified supernovae according to the public TNS classifications: ZTF19abpvbzf (SN IIn; Brennan et al. 2019), ZTF22aanwibf (SN II; Pellegrino et al. 2022). We also recovered the TDE ZTF21aaaokyp = AT2021axu (Hammerstein et al. 2021; Yao et al. 2023a), which we discard as it is not ambiguous.

The remaining events are detailed in Table 3. ZTF22aadesap = AT2022fpx (Perez-Fournon et al. 2022): The spectra of ZTF22aadesap = AT2022fpx do not resemble the main classes of TDE defined by Arcavi et al. (2014) and Velzen et al. (2021) and the object has recently been identified as an extreme coronal line emitter (Koljonen et al. 2024). The classification is thus ambiguous, so we include ZTF22aadesap = AT2022fpx as an ANT.

Seven of the remaining nine transients have been observed spectroscopically, four of which have public classifications while the other three are presented here for the first time. ZTF19aailpwl=AT2019brs is an ANT (Frederick et al. 2021) and ZTF20abrbeie=AT2021lwx (Subrayan et al. 2023; Wiseman et al. 2023) passes our selection by construction. ZTF21abxowzx=AT2021yzu and ZTF20abgxlut are spectroscopically classified as AGN at $z = 0.419$ (Chu et al. 2021a) and $z = 0.257$ respectively, but the light curves are clearly transient: in Section 3.1, we classify these as ANTs.

Further to public classifications, we obtained spectra for three that we photometrically and visually classified as Transients: ZTF18aczpgwm=AT2019kn, ZTF19aamrjar, and ZTF20abodaps = AT2020afep. These spectra are described in detail in Section 3.1. We also obtained spectra for three events which we labelled as Unclear: ZTF19aaozooc, ZTF20aaqtncr, ZTF20aauowyg. We discuss these events in Section 3.2. Finally, ZTF18acvvudh and ZTF22aaaeons have to our knowledge not been spectroscopically observed. They are therefore not considered for the remainder of this analysis, but we include them in Table 3 for completeness.

After visual inspection and spectroscopic filtering, we retain seven ANTs which we term our 'photometrically selected' sample: ZTF18aczpgwm=AT2019kn, ZTF19aailpwl=AT2019brs, ZTF19aamrjar, ZTF20abodaps=AT2020afep, ZTF20abrbeie=AT2021lwx, ZTF21abxowzx=AT2021yzu, ZTF22aadesap = AT2022fpx. We supplement these seven by searching for events within ZTF that fail our photometric selection but have similar spectroscopic features that do not resemble TDEs or AGN.

2.3 Supplementary spectroscopic sample

Our method of selecting ANTs with smooth power-law declines excludes genuine transient events with re-brightening episodes. To supplement this sample, we search for transients that have ANT-like light curves without the smoothness criteria. To do so, we search the TNS for events that were observed spectroscopically and classified as AGN or type II superluminous supernovae (SLSNe-II) since ANT is not a well-defined spectroscopic class, and BFF is not a classification category in TNS. We inspect the light curves and spectra for ANT-like signatures: a nuclear location, a long-duration (> 300 d) light curve, and a spectrum with a blue continuum and strong Balmer emission lines. We find three ZTF-detected events that were not identified by our pipeline but that fit these criteria. Two of these have been published in the literature as ANTs (ZTF19aatubsj/AT2019fdr and ZTF20aanxcpf/AT2021loi), and one which has not (ZTF20acvfraq/AT2020adpi). We add these to our analysis sample.

3 A SAMPLE OF AMBIGUOUS NUCLEAR TRANSIENTS

Based on a photometric selection pipeline, we identify 58 long-duration, smooth, high-amplitude events. We classify 6 as unclear and 16 as transients, of which 5 are spectroscopically confirmed supernovae and one is a TDE. Of the remaining nine likely ANTs, seven have spectra that do not resemble supernovae or TDEs. We supplement these seven ANTs with three spectroscopically selected ANTs that have less smoothly evolving light curves. In this section, we focus on the properties of these 11 selected ANTs, which we denote our 'analysis' sample.

3.1 Individual objects

We begin here by describing the individual events, before analysing the sample as a whole in Section 3.3. For each object, we check for cross-matches in other surveys. For each survey, we describe the data source and reduction methods below. In all cases, we correct for Galactic reddening using the dust maps of Schlafly & Finkbeiner (2011) assuming a Fitzpatrick (1999) extinction law.

3.1.1 ATLAS

We cross-match the ZTF transient with the data base of the Asteroid Terrestrial-impact Last Alert System (ATLAS; Tonry et al. 2018; Smith et al. 2020) from which we obtain forced difference imaging photometry from the ATLAS webserver (Shingles et al. 2021)[8]. Given the slow nature of the ANT light curves, to maximize signal-to-noise we combine ATLAS data into 20-d bins in each of the *c* and *o* filters.

3.1.2 Pan-STARRS

We obtain difference imaging photometry from the Panoramic Survey Telescope and Rapid Response System (PanSTARRS; Chambers et al. 2016; Wainscoat et al. 2016; a description of the transient filtering in current operation of the twin Pan-STARRS system is described in Smartt et al. 2024).

3.1.3 Gaia

We obtain long-term, white-light *Gaia G*-band photometry from via *Gaia* Science Alerts (Hodgkin et al. 2021). These data are particularly useful for assessing past variability of a given source and are not used for parameter estimation therefore we do not perform a host galaxy subtraction.

3.1.4 WISE

We obtain mid-infrared photometry from the *Wide-field Infrared Survey Explorer* (*WISE*) spacecraft as part of the NEOWISE reactivation mission (Mainzer et al. 2011) from the NASA/IPAC infrared science archive (IRSA[9]). We obtain catalogued photometry in the $W1$ (3.4 μm) and $W2$ (4.6 μm) bands for the full duration of the NEOWISE reactivation all sky survey (i.e. since 2013, five years before the start of ZTF). For each transient, we average the flux in each band over the period before the first optical detection and subtract this from post-optical-flare photometry.

3.1.5 VLASS

For each transient, we search the Karl G. Jansky Very Large Array Sky Survey (VLASS 2.1; Lacy et al. 2020) via the Canadian Astronomy Data Centre[10].

3.1.6 Swift

We search the archive of the *Neil Gehrels Swift Observatory* (*Swift*; Gehrels et al. 2004), and for five events obtained our own target of opportunity observations (PI: Wang). *Swift* X-ray data were taken in photon-counting mode with the X-ray Telescope (XRT; Burrows et al. 2005) and reduced with the tasks XRTPIPELINE and XSELECT. The source and background events were extracted using a circular region of 40 arcmin and an annular ring with inner and outer radii of 60 and 110 arcmin, respectively, both centred at the position of the source. The Ancillary Response Files were created with the task XRTMKARF and the Response Matrix File (RMF), swxpc0to12s6_20130101v014.rmf, was taken from the Calibration Data Base.[11] Targets were simultaneously observed with the Ultraviolet-Optical Telescope (UVOT; Roming et al. 2005) in the $uvw2$ (central wavelength, 1928 Å), $uvm2$ (2246 Å), $uvw1$ (2600 Å), u (3465 Å), b (4392 Å), and v (5468 Å) filters. The task UVOTIMSUM to sum all the exposures when more than one snapshot was included in each individual filter data and the task UVOTSOURCE to extract magnitudes from aperture photometry. A circular region of 5 arcmin centred at the target position was chosen for the source event, except for observations later than August 2023 after *Swift* experienced a jitter, and thus we use 8 arcsec – this affects ZTF18aczpgwm, ZTF19aamrjar, ZTF20abodaps, ZTF21abxowzx. Another region of 40 arcsec located at a nearby position was used to estimate the background emission. We have not performed a host subtraction on the UVOT data. In cases, where the UVOT data are used to constrain the black body SED, we verified that fits are consistent with and without the UVOT data.

We search for the spectra in the following public archives: the European Southern Observatory (ESO) Science Portal.[12], the Keck Observatory Archive[13], the Gemini Observatory Archive[14], and the Gran Telescopio CANARIAS Public Archive.[15]

Light curves for the analysis sample of eight photometrically selected ANTs are shown in Fig. 3 and the three spectroscopically selected are shown in Fig. 4. To convert to absolute magnitude for the figures, we include a $1+z$ correction to preserve flux density, but have not K-corrected to the rest frame g and r bands. Spectra are displayed in Fig. 5. Close-ups of the He II–[O III]–H β region (4500–5200 Å) and the Hα region (6300–6700 Å) is shown in Fig. 6.

3.1.7 Photometrically selected ANTs

ZTF20abrbeie/AT2021lwx/ATLAS20bkdj/PS22iin, $z = 0.9945$. First reported by ZTF via the AMPEL broker. This event was analysed in Wiseman et al. (2023) and Subrayan et al. (2023). The light curve is smooth and reaches $M_B \sim -25.7$, rising (in the rest frame) for over > 100 d and declining smoothly for over 450 d. It remains anomalous amongst the sample presented in this paper in having no detected host galaxy. The spectra displays broad and narrow Balmer emission lines, semi-forbidden carbon C II] and C III], and Mg II. There are no forbidden oxygen lines. A MIR flare is present with a ~ 1 yr rise and subsequent decline. X-rays are detected from the source, consistent with a power law and inconsistent with extrapolation of the UV-optical black body.

ZTF19aamrjar/ATLAS19mmu, $z = 0.697$. First reported by this work, ZTF19aamrjar has lasted just short of 1000 d in the rest frame since the first detection by ZTF, with a rise and decline timescale greater than that of AT2021lwx.[16] There is an MIR flare evolving slower than the optical, which has lasted 2 yr and not yet reached its peak.

This object was observed with the Las Cumbres Observatory (LCO Brown et al. 2013) Floyds spectrograph mounted on the 2 m Faulkes Telescope North in Haleakala, USA. The spectrum was reduced

[8] https://fallingstar-data.com/forcedphot/
[9] https://irsa.ipac.caltech.edu/Missions/wise.html
[10] https://www.cadc-ccda.hia-iha.nrc-cnrc.gc.ca/en/vlass/
[11] https://heasarc.gsfc.nasa.gov/docs/heasarc/caldb/swift
[12] https://archive.eso.org/scienceportal/home
[13] https://www2.keck.hawaii.edu/koa/public/koa.php
[14] https://archive.gemini.edu/
[15] https://gtc.sdc.cab.inta-csic.es/gtc/index.jsp
[16] Since the initial sample selection and analysis was conducted, ZTF19aamrjar has shown a secondary rise, indicating either more persistent accretion consistent with the quasar-like spectrum or a rebrightening from the transient. Such rebrightenings further blur the line between ANTs and AGN.

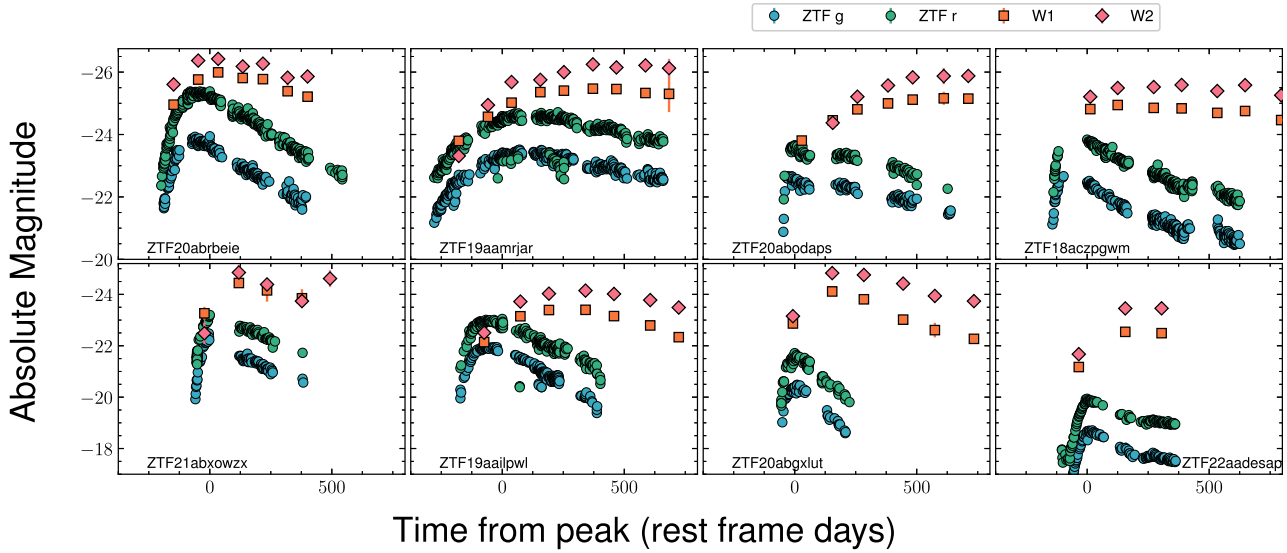

Figure 3. Optical and MIR light curves of the 8 photometrically selected ANTs passing 'gold' cuts and with spectroscopic redshift. The g, $W1$, and $W2$ bands have been shifted arbitrarily for clarity.

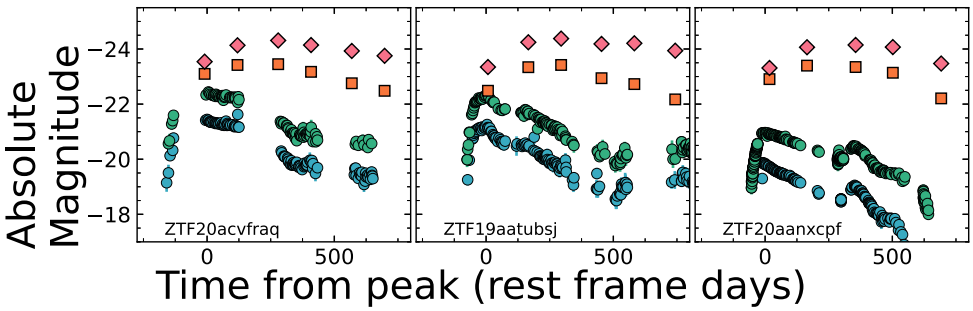

Figure 4. Optical and MIR light curves of the three spectroscopic ANTs with non-smooth light curves. The g, $W1$, and $W2$ bands have been shifted arbitrarily for clarity.

using the `floyds_pipeline` (Valenti et al. 2014).[17] It was also observed with the Optical System for Imaging and low-Intermediate-Resolution Integrated Spectroscopy (OSIRIS; Cepa et al. 2000) on the 10.8 m Gran Telescopio Canarias (GTC) at Observatorio del Roque de los Muchachos, La Palma, Spain. The spectrum was acquired in long-slit mode. The data were reduced via the PYPEIT package (Prochaska et al. 2020a, b). The spectra show strong Balmer and Mg II emission at $z = 0.697$. The Balmer lines (H β–H ϵ) are very broad with full-width at half maximum (FWHM) of $\sim 6200\,\mathrm{km\,s^{-1}}$. The line profiles are asymmetric with red wings. [O II] and [O III] are strong and narrow. There is Fe II emission redwards of 5000 Å. The spectrum is similar to highly luminous quasars with peculiar line profiles that have been identified as candidate recoiling or binary quasars (Eracleous et al. 2012; Shapovalova et al. 2016).

ZTF19aamrjar was observed with *Swift* on MJD 60241.01 ($t_{\rm max}$ + 634 d) for 2670 s. The X-ray spectrum is a power law with a photon index of 1.8 ± 0.9 and a flux of $4.4 \pm 2.5 \times 10^{-13}\,\mathrm{erg\,cm^{-2}\,s^{-1}}$ in the 0.3–10 keV range, corresponding to a luminosity of $9.5 \pm 5.4 \times 10^{44}\,\mathrm{erg\,s^{-1}}$.

ZTF20abodaps/AT2020afep/ATLAS20vrw, $z = 0.607$. First reported by ePESSTO + in this work. No previous variability in PS1 or PTF. The contrast between rise and decline time-scales is extreme: the light curve rises to -24 mag in ~ 30 d and declines constantly in 600 d. Observed with LCO Floyds on FTN and via the European Southern Observatory (ESO) as part of the extended Public ESO Spectroscopic Survey of Transient Objects (ePESSTO + ; Smartt et al. 2015) using the ESO Faint Object Spectrograph and Camera (EFOSC2; Buzzoni et al. 1984) on the New Technology Telescope (NTT) at ESO La Silla observatory, Chile. The EFOSC2 spectrum was reduced using the PESSTO pipeline (Smartt et al. 2015) v.3.0.1. The spectrum shows somewhat broadened Balmer lines (H β–H δ) at $z = 0.607$, along with Mg II. There is no detection of [O II] or [O III], similar to AT2021lwx.

Similarly to ZTF19aamrjar, ZTF20abodaps/AT2020afep has an MIR flare evolving slower than the optical, which appears to have reached peak brightness 2 yr after the optical peak.

X-ray observations were obtained on MJD 60263.67 ($t_{\rm max}$ + 738 d) with an exposure of 2367 s. X-rays are marginally detected. We find an upper limit of $f_{0.3-10\,\mathrm{KeV}} < 1.5 \times 10^{-13}\,\mathrm{erg\,cm^{-2}\,s^{-1}}$ when assuming a power law with index $\gamma = 1.8$ and a foreground absorption of $2.2 \times 10^{20}\,\mathrm{cm^{-2}}$. This limit corresponds to a luminosity of $L_{0.3-10\,\mathrm{KeV}} < 2.3 \times 10^{44}\,\mathrm{erg\,s^{-1}}$.

ZTF18aczpgwm/AT2019kn/ATLAS19bdfo/Gaia19abv, $z = 0.4279$. First reported by *Gaia* Science Alerts, the decline rate

[17] https://github.com/LCOGT/floyds_pipeline

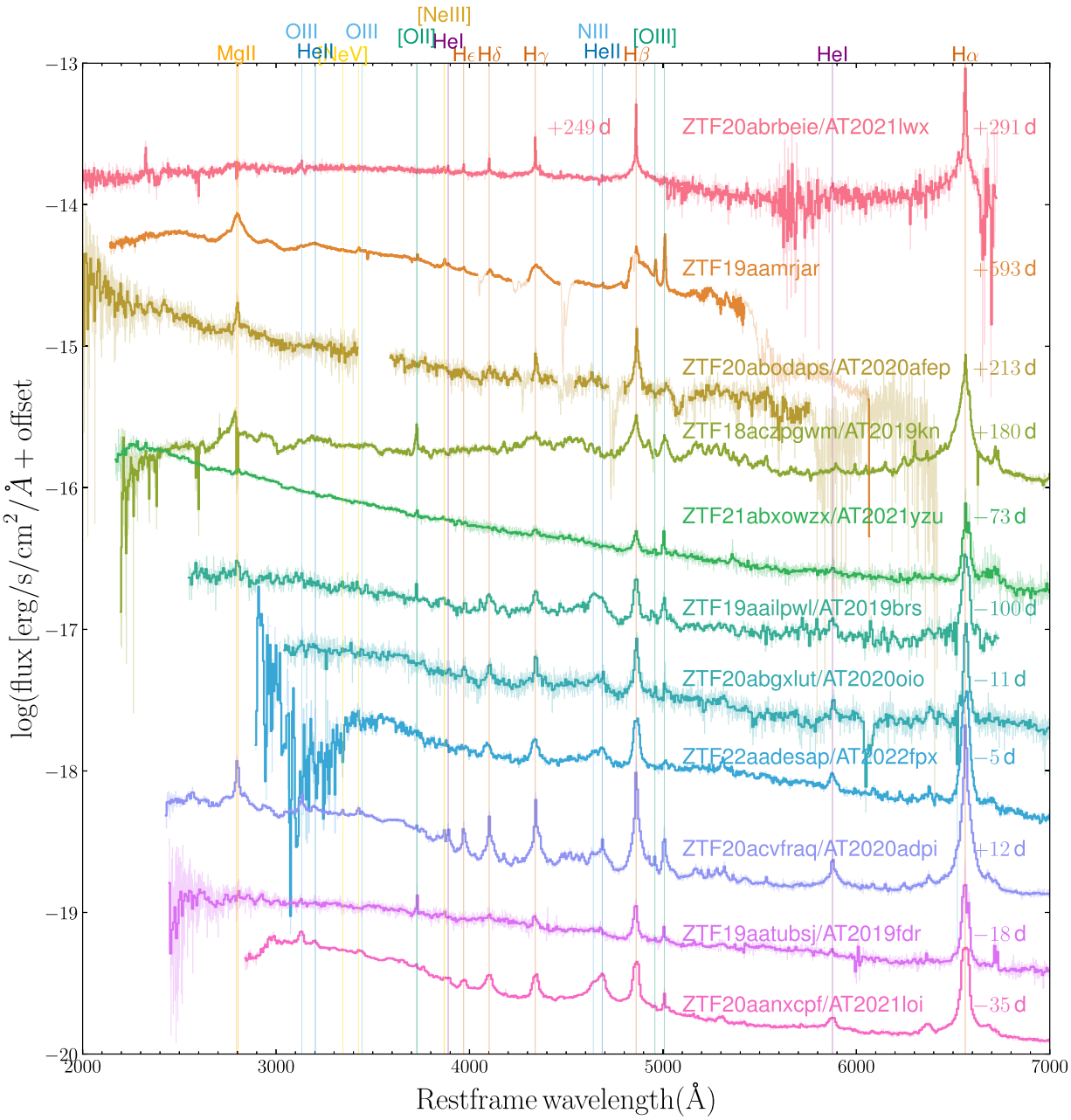

Figure 5. Rest-frame UV-optical spectra of the 11 ANTs in the analysis sample. Spectra are logged before scaling to preserve colour. Data are presented at original resolution (light shading) as well binned to 2.5 Å resolution for aesthetics (dark line), except ZTF20aaqtncr/AT2021fez which is binned to 7.5 Å due to the low signal to noise.

is very similar to AT2021lwx. A slight rebrightening occurred at + 450 d.

We obtain two publicly available spectra[18] from the Keck Low Resolution Imaging Spectrometer (LRIS; Oke et al. 1995) at the W. M. Keck Observatory, Hawaii, USA. The spectra were reduced using the LPIPE pipeline (Perley 2019) with default settings. The spectrum displays strong emission lines of the Balmer series and Mg II at $z = 0.4279$, as well as broad forbidden lines of [O III] and narrow lines of [O II], O I, and [S II]. The low-ionization lines (broad and narrow) show asymmetric profiles with a strong blue wing, indicating outflowing material. The presence of strong Fe II emission indicates a hot ionizing UV continuum. In addition, high-ionization 'coronal' iron lines are present from [Fe VI] and [Fe VII]. The spectrum suggests an underlying AGN similar to an NLSy1.

The MIR flare rises for $\sim$ 1 yr, followed by a plateau lasting $>$ 3 yr.

X-ray observations were obtained on MJDs 60262.82 and 60264.41 ($t_{\rm max}$ + 1134 d and +1136 d) with exposures of 1183 and 2580 s, respectively. We find an upper limit of $f_{0.3-10\,\rm KeV} < 8 \times 10^{-14}$ erg cm^{-2} s^{-1} when assuming a power law with $\gamma = 1.8$ and an absorption of 6×10^{20} cm^{-2}. This limit corresponds to a luminosity of $L_{0.3-10\,\rm KeV} < 5.3 \times 10^{43}$ erg s^{-1}.

[18]Program IDs C252,C253; PI: Graham.

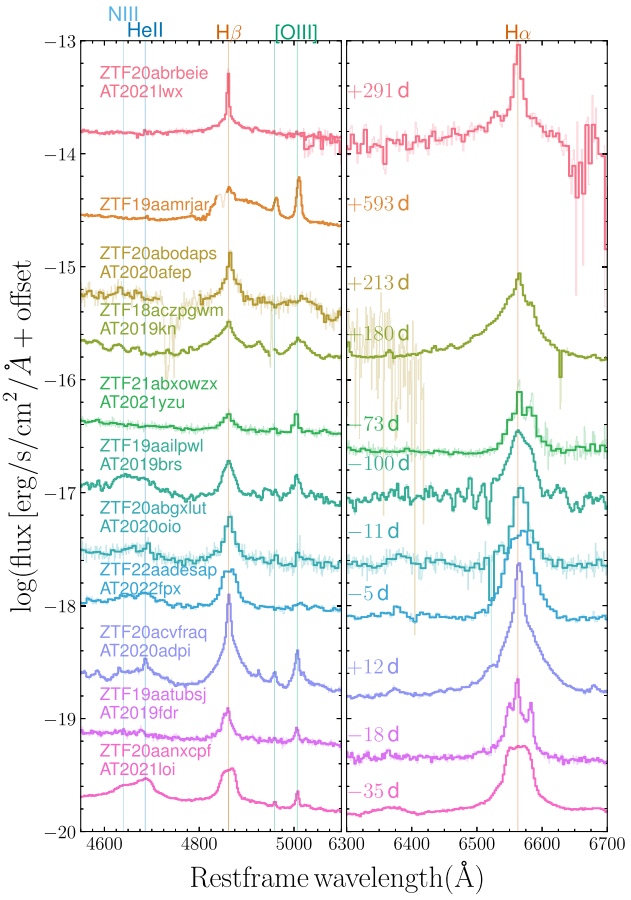

Figure 6. Left: The H β [O III] complexes, also covering the He II and N III lines. Right: The H α line, where available. These spectra are identical to Fig. 5, and have not been continuum subtracted.

ZTF21abxowzx/AT2021yzu/ATLAS21bjhp, $z = 0.419$. First reported by ZTF, classified as an AGN (Chu et al. 2021b). A bona-fide flare, this event occurred in a galaxy with no previous variability and with pre-flare MIR colours (*WISEW*1–*W*2 versus *W*3–*W*4) not consistent with AGN activity.

We retrieve a Keck/LRIS spectrum from the Weizmann Interactive Supernova Data Repository (WISeREP; Yaron & Gal-Yam 2012).[19] The spectrum is the bluest of the sample and somewhat resembles a type I AGN (Vanden Berk et al. 2001). It has broadened Balmer and Mg II, narrow [O II] and [O III], and hints of Fe II.

There is an MIR flare with a time-scale comparable to the optical light curve.

X-ray observations were obtained on MJDs 60243.54, 60248.44, and 60249.15 ($t_{\rm max} + 495$ d, +499 d, and +500 d), with exposures of 2244, 1138, and 1518 s, respectively. We place an upper limit of $f_{0.3-10\,\rm KeV} < 7.7 \times 10^{-14}$ erg cm^{-2} s^{-1} when assuming a power law with photon index 1.8 and an absorption of 3×10^{20} cm^{-2}. This limit corresponds to a luminosity of $L_{0.3-10\,\rm KeV} < 4.9 \times 10^{43}$ erg s^{-1}.

ZTF19aailpwl/AT2019brs/Gaia19axp, $z = 0.3736$. First reported by *Gaia* Science Alerts. Presented in the ANT sample of Frederick et al. (2021). The light curve is similar to AT2021lwx, although less luminous ($M_B \sim 24$) and with a faster (~ 50 d) rise followed by a plateau and a similar gradient decline.

[19] https://www.wiserep.org/

The event occurred in a known NLSy1. The spectrum (retrieved from WISeREP) shows strong narrow Balmer emission along with He II and N III characteristic of Bowen fluorescence flares.

An MIR flare is present with a lag of ~ 1 yr at peak.

There is extensive *Swift* coverage of this event with observations grouped in two broad epochs: MJD 58550–58850 ($t_{\rm max} - 95$ to +122 d) and MJD 59890–60020 ($t_{\rm max} + 880$ d to +975 d). There are no significant detections from each individual epoch, but grouping in the two above-defined bins reveals detections: assuming a power law with $\gamma = 1.8$ and Galactic absorption of 6×10^{20} cm^{-2}, the fluxes are $3.3 \pm 1.2 \times 10^{-14}$ and $7.7 \pm 4.9 \times 10^{-14}$ erg cm^{-2} s^{-1} corresponding to luminosities of $1.6 \pm 0.6 \times 10^{43}$ and $3.7 \pm 2.4 \times 10^{43}$ erg s^{-1}.

ZTF20abgxlut/AT2020oio/Gaia20dvv/ATLAS20rmk, $z = 0.257$. First reported by ZTF via the AMPEL broker. Initially classified as an AGN (Terreran et al. 2020), there is no evidence for any variability in pre-existing data.

The transient spectrum (retrieved from WISeREP) is almost identical to ZTF19aailpwl/AT2019brs, except although the He II, N III as well as [O III] are all present, they are all weaker in ZTF20agbxlut.

The pre-flare MIR colours (*WISEW*1–*W*2 versus *W*3–*W*4) are not consistent with AGN activity, and there is a clear MIR flare that lags the optical transient. There are no *Swift* X-ray observations of this event.

ZTF22aadesap/AT2022fpx/ATLAS22kjn/Gaia22cwy/PS23bdt, $z = 0.073$. First reported by ATLAS, this is the lowest luminosity event in our sample, showing an initially faster rise and decline followed by a quasi-plateau at later times.

ZTF22aadesap was classified as a TDE by Perez-Fournon et al. (2022) but then identified as an ECLE by Koljonen et al. (2024). While ECLEs have been observed in the late time stages of TDEs (Newsome et al. 2024), the peak spectrum of ZTF22aadesap/AT2022fpx does not resemble the common classes of TDE (e.g. Arcavi et al. 2014).

X-ray observations do not show a signal during the optical peak, but a strong late-time flare is observed at the same time as the optical date plateau. The implications of these observations are discussed in Koljonen et al. (2024).

3.1.8 *Spectroscopically selected ANTs*

ZTF20acvfraq/AT2020adpi/ATLAS20bjzp/Gaia21aid, $z = 0.26$. First reported by ZTF via the AMPEL broker. The rise time is uncertain due to gaps in the observed light curve, constrained to $40\,{\rm d} < t_{\rm rise} < 125$ d in the rest frame. The initial decline is shallow, before a steep phase and then a second shallow phase.

We obtain a Keck/LRIS spectrum from WISeREP. The spectrum is similar to ZTf19aailpwl/AT2019brs: dominated by strong Balmer lines with broad (FWHM= 3000 km s^{-1} and narrow components, along with He I and Mg II with similar profiles. Similarly to ZTF19aailpwl/AT2019brs is the presence of He II, N III, and a particularly strong O IIIλ 3312 line. These features indicate Bowen fluorescence. Fe II features can also be seen in the spectrum.

An MIR flare is present with a lag of ~ 1 yr at peak. *Swift* observed the location of the transient over the period of a month around the optical peak.

Swift XRT observed this event eight times between MJD 59 411 and 59 456 ($t_{\rm max} + 20$ to $t_{\rm max} + 56$ d). In a total of 9.4 ks, no X-rays are detected. Assuming a power law with photon index 2, this corresponds to an upper limit of 7.670×10^{-14} erg s^{-1} cm^{-2}, which equates to a luminosity limit $L_X < 1.6 \times 10^{43}$ erg s^{-1}.

ZTF19aatubsj/AT2019fdr/ATLAS19lkd/PS19dar/Gaia19bsz, $z = 0.2666$. First reported by ZTF via the AMPEL broker. Classified as a TDE in an NLSy1 (Frederick et al. 2021; Reusch et al. 2022), and although Pitik et al. (2022) classify it as a SLSN-IIn, we favour an SMBH-related interpretation.

The light curve is not smooth: the rise displays a 'shoulder' before peaking after 70 d, while after 70 d of steep decline there is an 80 d plateau before a shallower decline. After 500 d, a 0.7 mag rebrightening occurred and the transient has remained close to that level ever since.

We retrieve the Keck/LRIS spectrum from WISeREP. The Balmer emission is the most prominent feature, and there is weak but clearly detected He II.

There is an MIR flare with a lag at peak of ~ 300 d. The spectrum has narrow +broad Balmer emission lines as well as Fe II emission. There is no clear detection of He II or Bowen fluorescence lines. An MIR flare is present with a lag of ~ 1 yr at peak.

X-ray observations are presented in detail by Reusch et al. (2022). The event was observed by *Swift*-XRT with upper limits from observations in the first 315 d reaching $f_{0.3-10\,\mathrm{KeV}} < 1.4 \times 10^{-13}\,\mathrm{erg\,cm^{-2}\,s^{-1}}$. However, there is a late time detection of soft X-rays (0.3–2.0 KeV) from the *eROSITA* telescope (Predehl et al. 2021) on board the *Spectrum-Roentgen-Gamma* spacecraft (Sunyaev et al. 2021) at MJD 59283.

ZTF20aanxcpf/AT2021loi/ATLAS21qje, $z = 0.083$. First reported by *Gaia* Science Alerts. This event was analysed by Makrygianni et al. (2023) as a Bowen fluorescence flare. It is the second lowest luminosity of our sample ($L_{\mathrm{BB,max}} = 10^{44}\,\mathrm{erg\,s^{-1}}$). It has a similar initial light curve shape to the majority of the analysis sample presented here, but displays a clear rebrightening after ~ 400 d in the rest frame.

The spectrum, from Keck/LRIS and obtained from WISeREP, is similar to ZTF19aailpwl/AT2019brs and ZTF20acvfraq/AT2020adpi in that it is dominated by Balmer lines with an unusual flat-topped shape. There are strong emission lines from He II, N III, and O IIIλ 3312, indicating Bowen fluorescence and thus a very hot ionizing source. Any Fe II contribution is much weaker than in some of the Fe-strong events, but here the Balmer continuum is stronger.

A MIR flare is present with a lag of ~ 1 yr at peak.

Makrygianni et al. (2023) report X-ray upper limits from *Swift-XRT* of $L(2-10\,\mathrm{keV}) < (2.4-7.8) \times 10^{42}\,\mathrm{erg\,s^{-1}}$.

3.2 Unclear events

ZTF19aaozooc/AT2021hum/ATLAS20bjat, $z = 1.097$. The position of ZTF19aaozooc was targeted as part of the quasar survey (Richards et al. 2002) in the Sloan Digital Sky Survey (York et al. 2000). The spectrum, taken on MJD 52 028 (19 yr before the ZTF flare) and retrieved from SDSS data release 17 (Abdurro'uf et al. 2022), is of a type I quasar with broad Mg II, C III] and C IV. A further spectrum of ZTF19aaozooc was taken with Keck/LRIS around peak of the ZTF light curve (MJD 58788). The LRIS spectrum is qualitatively similar to the SDSS spectrum. We conclude that ZTF19aaozooc is a type I quasar with slow high-amplitude variability.

ZTF20aaqtncr/AT2021fez/ATLAS20pzv/Gaia21bgs, $z = 0.368$. First reported by *Gaia* Science Alerts. The light curve has a smooth rise and decline of similar duration, although the ZTF data release photometry (without difference imaging) shows variability before the transient detection. A spectrum was obtained with LCO Floyds FTN. The spectrum shows strong narrow Balmer emission lines, strong [N II], and very strong [O III]. The [O III]/H β ratio alone is enough to place the ionizing source as an AGN, which is confirmed by placing the line fluxes in the [O III]/H β versus [N II/H α] Baldwin–Phillips–Terlevich (BPT) diagram (Baldwin, Phillips & Terlevich 1981): $\log(NII/\mathrm{H}\alpha) = 0.01$, $\log(OIII/\mathrm{H}\beta = 0.86$. An MIR flare follows the optical rise, but does not follow the decline. A lack of broad Balmer features suggests this event is a high amplitude variability from a type II (obscured) AGN, a population which tend to show smaller amplitude variability over large time-scales (De Cicco et al. 2022). Nevertheless, such events could represent highly obscured examples of the more bonafide accretion transients and should be followed up with interest.

3.3 Sample properties

In this section, we present properties of the 11 selected ANTs measured from their light curves and spectra.

3.3.1 Black body properties

To estimate bolometric properties of the events, we model the observer-frame optical light curves as black bodies with evolving radii and temperatures using SUPERBOL (Nicholl 2018).[20] The resulting values are estimates that rely on several assumptions, namely that the emission is well described by a black body, in particular that it is spherically symmetric and that thermal processes dominate over non-thermal emission. For three events, the presence of soft X-rays inconsistent with the UV-optical black body indicates either non-thermal emission or multiple black body emission regions. Likewise, the majority of the events show a delayed-onset mid-infrared (MIR) flare consistent with the dust echo mechanism (see Section 3.3.3). Black body measurements are presented in Table 4. The ANTs have peak black body luminosities in the range $44.7 \leq \log(L_{\mathrm{BB,max}}/\mathrm{erg\,s^{-1}}) \leq 45.85$, and are thus among the most luminous transient astrophysical phenomena known, in particular more luminous than canonical TDEs (Yao et al. 2023a). We integrate the black body luminosities over the full observed light curve[21] to obtain the total radiated energy $E_{\mathrm{rad,BB}}$. The inferred energies are ten times greater than the most energetic supernovae (e.g. Nicholl et al. 2020) and three times the most energetic TDEs (Leloudas et al. 2016; Andreoni et al. 2022), and are firmly in the $E_{\mathrm{rad}} > 10^{52}$ erg regime of the heterogeneously compiled ANTs in the literature (e.g. Leloudas et al. 2016; Graham et al. 2017; Kankare et al. 2017; Oates et al. 2024).

3.3.2 Spectroscopic properties

The ANT spectra are clearly distinct from those of TDEs, which are dominated by blue continua and low equivalent width broad emission lines – some show only H, while others show H + He, He alone, Bowen fluorescence lines and Fe, or are 'featureless' (Arcavi et al. 2014; Leloudas et al. 2019; Velzen et al. 2021; Charalampopoulos et al. 2022). Our 11 ANTs are more AGN-like than TDE-like, consistent with the majority of ANTs in the literature. ANTs have narrower emission lines of higher equivalent width. Balmer lines of H are ubiquitous and have narrow and broad components, but the broad components are not as broad as those in TDEs: the mean H β width from our 11 ANTs is $\sim 2900\,\mathrm{km\,s^{-1}}$

[20] https://github.com/mnicholl/superbol

[21] Note that some events are still ongoing, thus the energies are listed as lower limits.

Table 4. Properties of the transients presented in this sample. log $L_{\rm bol,max}$, log $T_{\rm BB,max}$, and log $R_{\rm BB,max}$ are the luminosity, temperature, and radius assuming a black body, fitted to the optical data at the peak of the optical light curve. Uncertainties are statistical only. log $E_{\rm rad}$ is the radiated energy from the black body integrated over the observed light curve, with upper limits where the object is still visible. H β widths are FWHM and given for broad (b) and narrow (n) components.

ZTF ID	IAU name	$t_{\rm rise}$ (d)	log($L_{\rm BB,max}$) (erg s^{-1})	log($T_{\rm BB,max}$) (K)	log($R_{\rm BB,max}$) (cm)	log($E_{\rm rad,BB}$) (erg)	Hβ (b) (km s^{-1})	Hβ (n) (km s^{-1})	log($L_{r,\rm host}$) (erg s^{-1} Å^{-1})
ZTF20abrbeie	AT2021lwx	198	45.9 ± 0.1	4.0 ± 0.1	16.5 ± 0.1	> 53.3	2560[a]	250	–
ZTF19aamrjar	–	377	45.6 ± 0.4	4.2 ± 0.1	16.0 ± 0.1	> 53.7	6200[b]	732	41.5
ZTF20abodaps	AT2020afep	17	45.3 ± 0.5	4.0 ± 0.1	16.1 ± 0.2	> 53.1	1540		40.7
ZTF18aczpgwm	AT2019kn	125	45.2 ± 0.5	4.0 ± 0.03	16.2 ± 0.05	52.7 ± 0.2	2831[c]	245	40.6
ZTF21abxowzx	AT2021yzu	71	45.3 ± 0.5	4.3 ± 0.03	15.7 ± 0.03	52.4 ± 0.1	1690	194	40.2
ZTF19aailpwl	AT2019brs	173	45.0 ± 0.1	4.2 ± 0.01	15.7 ± 0.02	52.5 ± 0.1	2650	1000[e]	40.4
ZTF20abgxlut	AT2020oio	96	44.2 ± 0.2	4.0 ± 0.04	15.7 ± 0.06	51.3 ± 0.4	3800	970	39.4
ZTF22aadesap	AT2022pfx	103	43.7 ± 0.1[g]	4.1 ± 0.02	15.2 ± 0.04	51.1 ± 0.1	2100		39.4
ZTF20acvfraq	AT2020adpi	120	44.6 ± 0.2	4.0 ± 0.04	15.9 ± 0.08	52.3 ± 0.1	3830	537	39.9
ZTF19aatubsj	AT2019fdr	77	44.6 ± 0.1	4.0 ± 0.03	15.9 ± 0.05	52.1 ± 0.3	4100[f]	370	40.1
ZTF20aanxcpf	AT2021loi	59	44.0 ± 0.1	3.9 ± 0.01	15.8 ± 0.02	51.4 ± 0.1	2150		39.5

Note. [a]Revised from Wiseman et al. (2023) based on higher quality data. An additional broad component with FWHM~ 12000 km s^{-1} is also compatible with the data; [b]the broad line is highly asymmetric and affected by imperfect telluric subtraction; [c]there may be an even broader component with FWHM$\sim 1.2 \times 10^4$ km s^{-1} but this may be caused by unmodelled Fe II emission; [d]Formally unconstrained due to only two available filters constrain blackbody model; [e]consistent with the pre-flare measurement from an SDSS spectrum (Frederick et al. 2021); [f]the significance of this component is dependent upon the continuum modelling; [g]using *gri* only as opposed to Koljonen et al. (2024) who add *Swift* UV data.

(Table 4) compared to $> 10^4$ km s^{-1} for TDEs (Charalampopoulos et al. 2022). Eight out of 11 ANTs have clear narrow [O III] λ5007 which is a tracer of low-density ionized gas and present in both AGN and star-forming galaxy spectra (Osterbrock 1989; Vanden Berk et al. 2001). It is lacking in the spectra of ZTF20abrbeie/AT2021lwx and ZTF20abodaps/AT2020afep. The ratio of this line to H β can be used to estimate whether the ionizing source is an AGN or star formation (Baldwin et al. 1981; Kewley et al. 2001; Kauffmann et al. 2003) while its absence indicates that neither AGN emission nor star formation are strong in the hosts of these transients.

3.3.3 *Mid-infrared lags*

All 11 events show changes in their MIR luminosity as measured in the *WISE* W1 (3.3 µm) and W2 (4.6 µm) bands. The light curve morphologies are varied, but all show a rise that is delayed from the optical flare. ZTF18aczpgwm, ZTF19aamrjar, ZTF20abodaps, ZTF20aaqtncr, and ZTF20aanxcpf show smooth ongoing rises. On the other hand, ZTF20abrbeie, ZTF19aailpwl, ZTF20acvfraq, and ZTF19aatubsj have MIR flares that peak within the timescale of the UV-optical light curve. MIR flares have been observed in TDEs (e.g. Velzen et al. 2016; Jiang et al. 2021b), BFFs and ANTs (e.g. Jiang et al. 2021a; Wiseman et al. 2023; Hinkle 2024) and are assumed to represent dust echoes from torus-like structures surrounding the black hole. The time lags between the UV-optical and MIR flares indicate the physical scale of the dust, the black body colour reveals its temperature, and the ratio of optical-to-MIR luminosity represents the dust covering fraction.

We present the observed lags between the g band and the $W1$, $W2$ light curves in Table 5. The lags are estimated at observer frame wavelengths but are corrected for time dilation. The roughly 6-month cadence of NEOWISE means that these lags are estimates, with uncertainty of $\pm$90 d. We present two lag measurements for each *WISE* band: the 'peak' lag, which is the time from g-band peak to the *WISE* peak; and the 'rise' lag, which we measure from the first rising optical detection to the first rising *WISE* detection. To estimate the time of peak brightness in each band, we fit the light curves with Gaussian process (GP) regression (Rasmussen & Williams 2005) implemented via the GEORGE package (Ambikasaran et al. 2015). We use the squared exponential kernel with a scale length optimized via gradient-based methods, as per Pursiainen et al. (2020). We constrain the MIR scale length to be greater than or equal to the optical, to account for the lower cadence of the MIR observations. In most cases, we find the $W1$ and $W2$ peaks to be consistent with one another (i.e. within the 90 d uncertainty). As described above, some events are yet to peak in the MIR such that their lags are lower limits.

To estimate the rise lags, we simply take the time between the first rising point in the optical and MIR. For the optical, we make use of ZTF forced photometry which often reveals rising light curves from before the first formal difference image detection. For the MIR, for which we do not have difference imaging, we estimate the host/AGN level by taking a weighted mean of the brightness before the first optical detection. None of the events show pre-flare variability in the MIR that is greater than the measurement uncertainties. The optical-MIR rise lag is then determined by the time of the first MIR point that lies significantly (i.e. (detection $-$ host) $>$ host uncertainty). In many cases, this lag is clearly an upper limit set by the WISE cadence.

3.3.4 *Dust properties*

We estimate the dust temperature, radius, and luminosity by fitting the host-subtracted $W1$ and $W2$ data with a black body SED. We infer a dust covering fraction as the ratio between the estimated dust luminosity and the UV-optical luminosity. Due to having only two *WISE* filters and no near IR, the blackbody temperatures are poorly constrained – formally the uncertainties are 100 per cent. Results are presented in Table 5. Our estimated dust properties are consistent with those measured for a sample of ANT MIR flares (Hinkle 2024). In particular, we compare the three events common to both samples (ZTF19aatubsj, ZTF20cvfraq, ZTF20aanxcpf) for which our temperature and effective radius measurements agree. The covering fractions are of similar magnitude to those reported by Hinkle (2024). We note that dust emission is not a perfect black body: the main effects of allowing for an absorption coefficient would be a shift to lower inferred dust temperatures and larger distances from

Table 5. Dust properties of the transients presented in this sample. Luminosity, temperature, and radius are measured at the MIR peak. A description of the various lags is provided in Section 3.3.3. Lags have an uncertainty of ±90 d due to the NEOWISE cadence.

ZTF ID	IAU Name	$W1_{\rm peak}$ lag d	$W2_{\rm peak}$ lag d	$W1_{\rm rise}$ lag d	$W2_{\rm rise}$ lag d	$\log(L_{\rm dust})$ erg s^{-1}	$\log(T_{\rm dust})$ K	$R_{\rm dust}$ pc	f_C	$\log(L_{\rm bol,pre})$ erg s^{-1}
ZTF20abrbeie	AT2021lwx	119	119	54	54	44.63	3.54	0.04	0.06	–
ZTF19aamrjar	–	472	472	25	25	44.55	3.28	0.09	0.09	44.9
ZTF20abodaps	AT2020afep	> 492	> 492	220	220	44.69	3.20	0.15	0.16	44.6
ZTF18aczpgwm	AT2019kn	> 197[a]	> 197[a]	77	77	44.42	3.30	0.07	0.17	44.4
ZTF21abxowzx	AT2021yzu	> 216[b]	100[b]	40	< 181	–	–	–	–	–
ZTF19aailpwl	AT2019brs	405	405	116	116	44.41	3.20	0.11	0.20	44.3
ZTF20abgxlut	AT2020oio	139	139	43	43	44.13	3.16	0.09	0.86	–
ZTF22aadesap	AT2022pfx	137	286	260	69	43.02	3.02	0.05	0.18	43.5
ZTF20acvfraq	AT2020adpi	305[c]	305[c]	160	160	44.18	3.12	0.12	0.38	–
ZTF19aatubsj	AT2019fdr	303	303	82	82	44.00	3.08	0.12	0.25	44.6
ZTF20aanxcpf	AT2021loi	173	364	70	70	43.59	3.14	0.06	0.39	43.1

Note. [a]MIR light curve has a ∼ 600 d plateau; [b]MIR detections are low significance and do not show a clear flare; [c]time of optical and MIR peaks uncertain.

the source to the dust (Jiang et al. 2021b), although neither of these affects our conclusions.

The effective dust temperatures lie within 1200 K < $T_{\rm dust,peak}$ < 2000 K which is consistent with the sublimation temperatures of graphite (1800 K) and silicate (1500 K) grains (Mor, Netzer & Elitzur 2009; Mor & Netzer 2012). Correlations between the various dust parameters, lags, as well as the H β widths and UV-optical black body luminosity are shown in Fig. 7. We also measure the black body temperatures and radii from averaged pre-flare MIR fluxes. Assuming this pre-flare emission is dominated by circumnuclear dust illuminated by a bright UV-optical source (i.e. accretion disc), we can estimate the luminosity of this source, which we do following Petrushevska et al. (2023). For the seven sources with pre-flare MIR flux, we verify that the inferred pre-flare luminosity is smaller than the peak UV-optical luminosity by ∼ 1 order of magnitude in each case.

We perform a simple Kendall τ test for correlation for all pairs of parameters. To determine which correlations are significant, we check for those with a p-value of 0.05 adapted for the look elsewhere effect for 50 parameter pairs, resulting in a p-value threshold of 0.001. Three pairs pass this threshold: the 'first' lags and peak lags, although we note that these two lag measurements are not correlated with each other. This is likely due to the 6-month NEOWISE cadence. We also recover a correlation between dust luminosity the UV-optical luminosity ($\tau = 0.85 p = 0.00064$), further evidence that the MIR emission is indeed a dust echo of the UV-optical flare.

We also note that the $W1$ and $W2$ peak lags appear tentatively correlated with the width of narrow H β ($\tau = 0.81 p = 0.01071$, with the high p-value due to some events not having a clear narrow feature) but not with that of broad H β. This may be evidence for the case where the narrow Balmer emission is caused by the reprocessing of kinetic energy of an outflow via the shock heating of a circumnuclear dust cloud, while the broad lines are from the outflow or accretion disc and thus do not correlate with the scale of the surrounding medium.

3.4 Summary of properties

In this section, we have presented 11 examples of ANTs with 1 yr light curves. Seven are photometrically selected and three spectroscopically. They are luminous with $L_{\rm BB} \geq 10^{44}$ erg s^{-1}; the six ANTs from the photometric selection that have constraints on their black body SEDs have $L_{\rm BB} \geq 10^{45.1}$ erg s^{-1}. All ANTs have strong high equivalent-width Balmer lines. These lines are narrow compared to TDEs. The mean FWHM of the broad component of H β in the ANTs is ∼ 2900 km s^{-1} whereas for TDEs, this is > 10^4 km s^{-1} (Charalampopoulos et al. 2022). All but one ANT has a strong MIR flare with a peak luminosity at least 10 per cent of the UV-optical black body luminosity, with temperature 1000–2000 K, with radius ∼ 0.1 pc and with a peak-to-peak lag from the optical > 100 d. All of these properties are consistent with a light echo from warm dust on the scales typically seen in AGN.

4 COMPARISONS BETWEEN THE VARIABILITY OF ANTS AND AGN

Distinguishing ANTs from the stochastic variability of AGN in a magnitude-limited photometric survey is non-trivial. An AGN that stays below the magnitude limit for several years and then fluctuates above that limit will mimic an ANT, which we assume is the case for 52/59 of the 'gold' candidates that do not show smooth light curve evolution, as well as for the rest of the ∼ 50 000 passing the initial cuts. The separation of ANTs from AGN in real time is challenging, and will become more so with the increased depth of future surveys such as the Vera C. Rubin Observatory's Legacy Survey of Space and Time (LSST; Ivezic et al. 2019). Here, we explore measures of light curve variability in order to learn how ANTs compare to the variability of typical AGN.

Variability of AGN is commonly described by a model-free *structure function* (SF; Hughes, Aller & Aller 1992; Bauer et al. 2009; Kozłowski 2016). The true SF, if observational noise has been accounted for, simply describes the root-mean-square variability about the mean AGN magnitude for a given time-scale $\Delta t = t_i - t_j$. The observed SF is

$$\mathrm{SF}(\Delta t) = \sqrt{2\sigma_{\rm s}^2 + 2\sigma_{\rm n}^2 - 2\mathrm{cov}(s_i, s_j)}\,, \quad (1)$$

where $\sigma_{\rm s}^2$ is the variance of the observed signal, $\sigma_{\rm n}^2$ is the noise, and $\mathrm{cov}(s_i, s_j)$ is the covariance between all data s_i, s_j for that time-scale Δt.

The SF can be parametrized by two power laws, with index $\gamma > 0$ for variability on time-scales Δt shorter than some break time τ, and $\gamma = 0$ at $\Delta t \to \infty$, i.e. that the amplitude of variability scales with timescale until τ where it becomes uncorrelated. The case of $\gamma = 2$ corresponds to the damped random walk (DRW): in this case, the SF can be described by the time-scale $\tau_{\rm DRW}$ and the amplitude of the SF as $\Delta t \to \infty$, denoted SF_∞. The general population of AGN show a positive correlation between $\tau_{\rm DRW}$ and SF_∞ (e.g. MacLeod

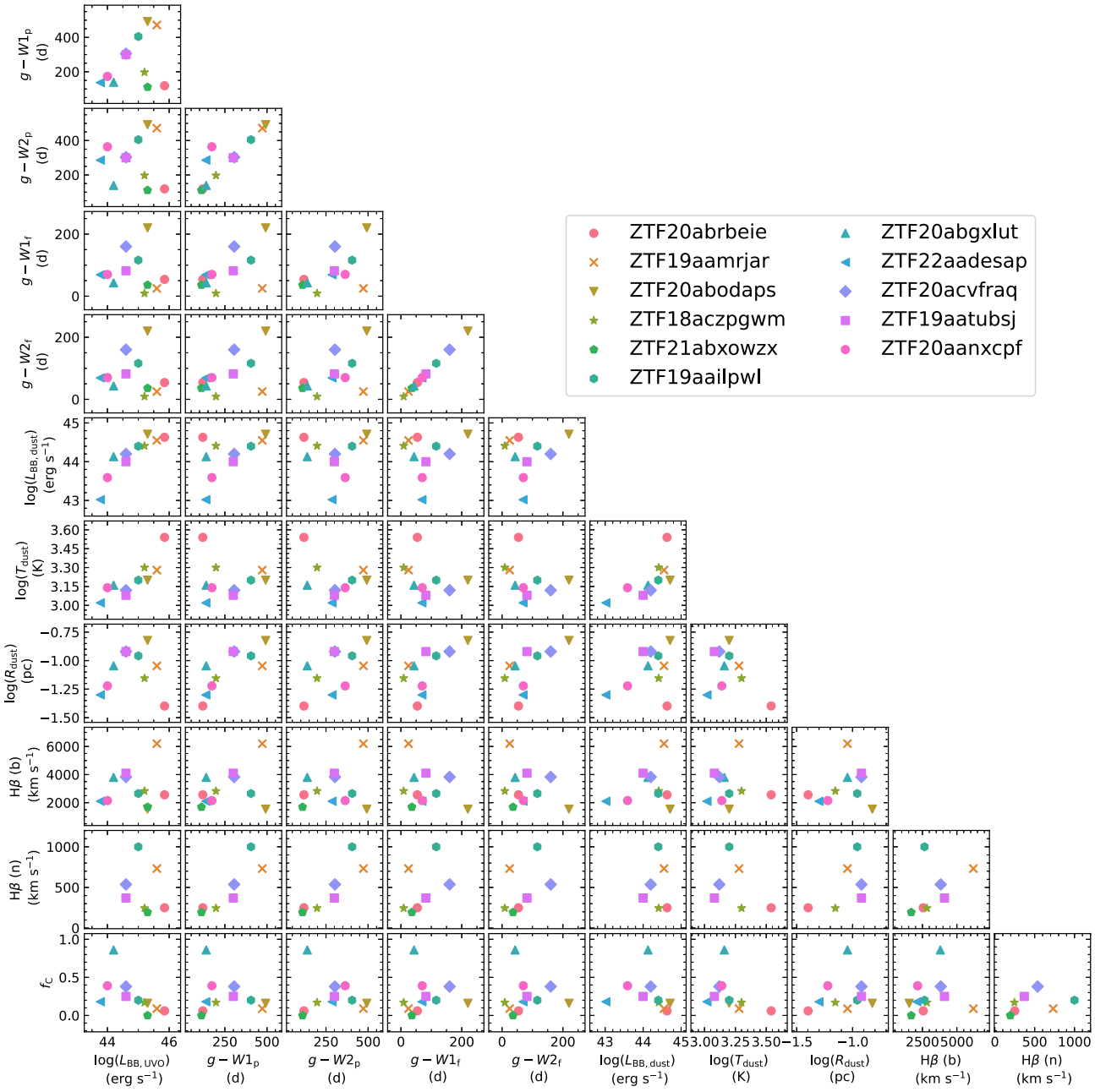

Figure 7. Correlations between optical flares, optical spectra, and dust light curves of the 11 ANTs in the analysis sample.

et al. 2010), such that objects with longer time-scales tend to display higher-amplitude long-term variability.

We assess the variability of the 11 ANTs in the analysis sample, the 59 'gold' candidates returned by our linear-decline, high-amplitude selection as well as the 'faster' and 'bumpier' samples. We also compute the SF for all ZTF nuclear transient candidates detected in the first year of ZTF, most of which are likely AGN. We restrict to these candidates so that we have at least a 5 yr baseline. Instead of the difference-imaging magnitudes, which amplify differences with respect to some baseline, we obtain photometry from the ZTF Public Data Release 22[22] (Masci et al. 2018) that includes any baseline AGN luminosity as well as the host galaxy contribution and can be compared directly to the well-studied SDSS sample. We fit the observer-frame r-band light curves with a DRW using the TAUFIT[23] package, fitting for the τ_{DRW} and SF_∞ parameters. In an ideal case, we would use rest frame light curves, but the majority of ZTF candidates do not have measured redshifts to allow for a K-correction. The results are shown in Fig. 8: SDSS AGN (MacLeod et al. 2010) and ZTF nuclear candidates are shown in blue and dark red contours, respectively, while the SFs for ANTs in our gold sample are shown in open gold diamonds, and the SFs for ANTs are shown in open green hexagons. In general, DRW fits are unreliable if the observed baseline is not significantly longer than τ_{DRW}. For the 7229 ZTF nuclear light curves, the maximum possible baseline is $\sim$ 1800 d,

[22] https://www.ztf.caltech.edu/ztf-public-releases.html

[23] https://github.com/burke86/taufit

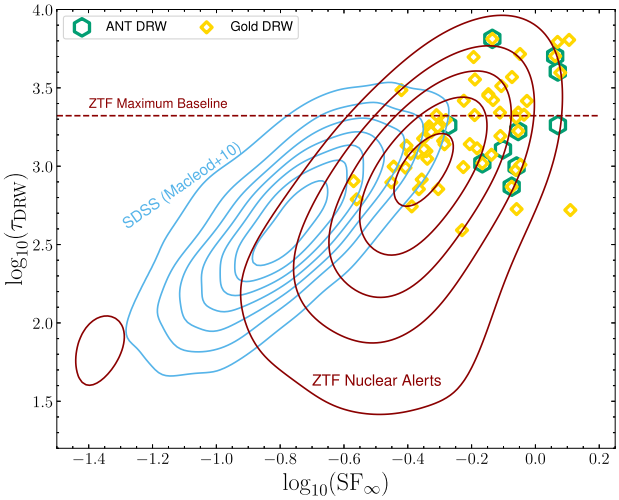

Figure 8. Structure function of AGN compared to the variability shown by light curves selected to be smooth and high amplitude. Structure functions for SDSS AGN and all ∼ 50 000 ZTF nuclear alerts are shown in contours. Structure functions assuming a damped random walk (DRW) for our analysis sample of 11 ANTs, plus the gold sample of 59, are shown in open markers.

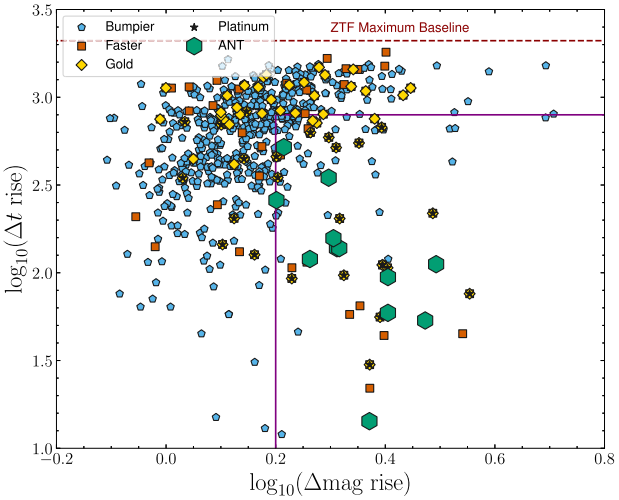

Figure 9. Rise times and rise amplitudes of all our sample variations. The box represents a selection of ANTs with 50 per cent purity against AGN-like light curves. Note the, *x*-axis is shifted to the right compared to Fig. 8.

indicated by a horizontal line in the figure. Results above this line are unreliable while results below the line could be lower limits since longer baselines were not measurable. The ZTF candidates are all shifted to higher amplitude $\rm SF_\infty$ compared to the SDSS AGN, likely because all of these events are transient candidates detected in difference imaging and thus must be variable above the ZTF detection limit in the difference image (the $5\,\sigma$ threshold at $m_{\rm r} \sim 20$ is about 0.6 mag.

4.1 Rise time versus amplitude

The 59 'gold' ANT candidates are selected to be smoothly evolving. Although the DRW is still a valid description of a low amplitude, long time-scale variability, it is far from an ideal model for such transient variability. Nevertheless, the resulting $\rm SF_\infty$ all lie to the upper edge of the contour from ZTF, and are (by selection) larger than almost all MacLeod et al. (2010) AGN. The analysis ANT sample is clearly shifted compared to the full 'gold' sample which includes objects with shorter τ and smaller $\rm SF_\infty$. To assess the significance of the largest flare, we measure the observer-frame rise time from first detection to peak brightness of the *r*-band light curve (not *K*-corrected) and plot these against the change in difference magnitude over the same time-scale. These are shown as filled points in Fig. 9, for the analysis sample of 11 plus the 'gold', 'bumpier', and 'faster' selections. These measurements clearly indicate higher amplitude variability than measured by the DRW, and indicate a shorter time-scale for that variability. There is a clear preference for the ANTs to have shorter rises from first detection to peak brightness compared to the 'gold', 'bumpier' and 'faster' samples. This is despite the 'faster' sample being selected for having a shorter decline, and indicates that most events picked up by that selection have slow rises and fast declines, indicative of stochastic variability rather than transient behaviour.

We construct a region in rise-time versus rise amplitude space that includes all 11 ANTs from the analysis sample. This region is bounded by $\log_{10}(\Delta\text{mag rise}) > 0.2$ (equivalent to 1.6 mag) and $\log_{10}(\Delta t \text{ rise}) < 2.9$ (equivalent to ∼ 800 d). We suggest that any light curves falling outside this range are likely due to stochastic AGN variability. Within this region are 9 'platinum' events that are not in our analysis sample. Of these, one is a peculiar TDE, two are SNe in a star-forming knots, and three are ANTs that pass our visual inspection but do not have spectra. Thus there are only 4 true AGN 'contaminants' when applying these selection criteria and we advocate their use in future surveys.

5 DISCUSSION

We have searched for analogues of the extremely luminous transient AT2021lwx and have systematically identified a further sample of slow and smoothly evolving nuclear transients in the ZTF data stream. Of these transients, only one (ZTF19aailpwl/AT2019brs) has been published as a transient of interest. Another, ZTF21abxowzx/AT2021yzu, was publicly classified as an AGN. With this pipeline, we identify four further events with photometric and spectroscopic properties consistent with ANTs. ZTF18aczpgwm/AT2019kn has broad high equivalent-width emission lines as well as very strong iron complex. ZTF19aamrjar is the longest-lived of the sample and has the highest integrated radiated energy. Its spectrum resembles a quasar and it has red-winged asymmetric Balmer lines, yet its photometric evolution is entirely smooth for over 2 yr in the rest frame. ZTF20aaqtncr/AT2021fez is a lower amplitude flare whose emission lines resemble a type II AGN. ZTF20abodaps/AT2020afep rises on the time-scale of a regular SN or TDE, but declines far, far slower. All of these transients display an MIR flare consistent with circumnuclear dust echoes.

We supplemented these ANTs with three others observed by ZTF that do not have linear declines but whose spectroscopic properties do not fall into other astrophysical classes. Despite the discontinuous light curve shapes, the derived properties appear similar: the spectral shapes, Balmer line widths, UV-optical pseudo-bolometric luminosities, and MIR flare characteristics are consistent with the linearly-declining sample.

5.1 TDEs, CLAGNs, or something in between?

The samples presented in this work add to a growing list of ANTs discovered in untargeted searches. Some previously published events (e.g. PS1-10adi, PS16dtm, Gaia16aaw, ASASSN-17jz, Gaia18cdj) have similar smooth rises and declines to the ZTF sample. On the other hand, another set of events show differing light curves with either fast rises, bumpy declines, or plateaus (e.g. ASASSN-15lh, OGLE17aaj, AT2017bgt, ASASSN-18jd, Swift J221951-484240). Nevertheless, all but ASASSN-15lh are spectroscopically similar, dominated by strong narrow Balmer emission lines (and ASASSN-15lh has been claimed to be a TDE by Leloudas et al. 2016). These observations indicate that slow-moving gas is nearly ubiquitous in ANTs but that the geometry and/or central energy source may not be, leading to the different light curve shapes.

The physical nature of each individual ANT, and the class as a whole, is unclear. Many possible scenarios have been extensively discussed in the literature, and we have shown that any such scenario must readily explain strong narrow emission, large radii, and high dust covering fractions. Here, we briefly address the most likely scenarios and how they relate to inferred properties of ANTs.

5.1.1 Extreme instability in an existing accretion disc

Arguably the most simple explanation of ANTs is an intrinsic change in the structure of an existing accretion disc (e.g. Sniegowska et al. 2020). The existence of the disc before the flare is required in many ANTs which are found in NLSy1 galaxies or other AGNs. This scenario is comprehensively addressed in Cannizzaro et al. (2020) where it is shown that the rise time-scales of ANTs (months) are far too short compared to the dynamical time-scale of a classical accretion disc (>70 yr), although see Lipunova, Tavleev & Malanchev (2024) for possible origins of flares due to thermal fluctuations in discs.

5.1.2 Tidal disruption in an existing accretion disc

One way of rapidly altering the accretion rate in an existing disc is via a TDE, a scenario proposed for many of the NLSy1 ANTs (e.g. AT2019fdr; Frederick et al. 2021; PS16dtm; Blanchard et al. 2017; Petrushevska et al. 2023; PS1-10adi; Kankare et al. 2017) as well as some CLAGNs (e.g. Merloni et al. 2015). Predictions for the properties of such events are sparse (McKernan et al. 2022; Prasad et al. 2024). Chan et al. (2019) show that the debris stream of a TDE interacts with the disc with a plethora of possible outcomes, dependent on the mass ratio of the debris and disc. They also indicate that a particularly heavy debris stream may hit the disc a second time, a possible explanation for the bumpier ANTs like ZTF19aatubsj/AT2019fdr and ZTF20aanxcpf.

5.1.3 Tidal disruption event of a massive star

The ANTs presented here are extremely luminous and long-lived, properties indicative of a massive SMBH central engine. Black hole masses in canonical TDEs are found to be 10^5–$10^7\,\mathrm{M}_\odot$ (Mockler, Guillochon & Ramirez-Ruiz 2019; Nicholl et al. 2022), and solar mass stars can only be disrupted by black holes $\lesssim 10^8\,\mathrm{M}_\odot$ (Hills 1975). Wiseman et al. (2023) and Subrayan et al. (2023) showed that the light curve ZTF20abrbeie/AT2021lwx could be modelled by a $\sim 15\,\mathrm{M}_\odot$ star disrupted by a $8 \times 10^8\,\mathrm{M}_\odot$ black hole, and Wiseman et al. (2023) claimed such an event was highly improbable due to the short lifetimes and low numbers of such massive stars.

Table 6. Black hole and stellar mass properties for the MOSFiT TDE model fit to 11 ANTs.

ZTF ID	IAU name	$\log_{10}(M_{\rm BH})$ $\mathrm{M}_\odot$	M_* $\mathrm{M}_\odot$
ZTF20abrbeie	AT2021lwx	$8.32^{+0.01}_{-0.01}$	$14.8^{+0.1}_{-0.3}$
ZTF19aamrjar	–	$8.69^{+0.01}_{-0.01}$	90^{+7}_{-5}
ZTF20abodaps	AT2020afep	–	–
ZTF18aczpgwm	AT2019kn	$7.5^{+0.05}_{-0.04}$	$9.8^{+3.7}_{-6.1}$
ZTF21abxowzx	AT2021yzu	$7.4^{+0.5}_{-0.7}$	$2.5^{+1.1}_{-1.7}$
ZTF19aailpwl	AT2019brs	$7.1^{+0.6}_{-0.4}$	$1.5^{+0.3}_{-0.2}$
ZTF20abgxlut	AT202oio	$7.04^{+0.15}_{-0.21}$	$0.28^{+0.22}_{-0.15}$
ZTF22aadesap	AT2022fpx	$7.46^{+0.12}_{-0.05}$	$\mathbf{1.38^{+0.64}_{-0.86}}$
ZTF20acvfraq	AT2020adpi	7.0 ± 0.1	$1.9^{+2.3}_{-0.8}$
ZTF19aatubsj	AT2019fdr	7.3 ± 0.2	$4.5^{+5.2}_{-2.7}$
ZTF20aanxcpf	AT2021loi	$6.5^{+0.3}_{-0.1}$	0.12 ± 0.07

Here, we fit the light curves of the analysis sample with the Modular Open Source Fitter for Transients (MOSFiT; Guillochon et al. 2018) using the TDE model of Mockler et al. (2019). We achieve reasonable fits to all the light curves except ZTF20abodaps/AT2020afep, for which the rise time is too fast compared to the decline time. The best-fitting stellar and black hole masses are presented in Table 6. The most eyecatching is ZTF19aamrjar, which requires $M_* \sim 90\,\mathrm{M}_\odot$ and $M_{\rm BH} = 5 \times 10^8\,\mathrm{M}_\odot$. Such a scenario is far beyond the scope of the MOSFiT models which derive from simulations of solar mass stars. All of the others have parameters more in line with what might be expected for extreme but plausible TDEs: $M_* < 3\,\mathrm{M}_\odot$ (with the exception of ZTF18aczpgwm/AT2019kn for which $M_* \sim 10\,\mathrm{M}_\odot$) and $M_{\rm BH} < 10^8\,\mathrm{M}_\odot$.

The mean black hole mass of our sample is $\log(M_{\rm BH}/\mathrm{M}_\odot) = 7.4$ with a standard deviation of 0.6 dex. We compare these masses to those of 32 TDEs fit using the MOSFiT TDE model in Nicholl et al. (2022), whose highest black hole mass is $\log(M_{\rm BH}/\mathrm{M}_\odot) = 7.2$ with a mean $\log(M_{\rm BH}/\mathrm{M}_\odot) = 6.6$. We perform a two-sample Kolmogorov–Smirnov (KS) test and conclude with a p-value of 0.0001 (i.e. 99.9 per cent, or $3.6\,\sigma$) that the ANT black hole masses are not drawn from the population of TDE black hole masses. We also compare to the 33 black hole masses of TDEs in Yao et al. (2023a) measured using the host galaxy bulge–black hole mass relation. Their mean mass is $\log(M_{\rm BH}/\mathrm{M}_\odot) = 6.5$ and although they extend to higher masses than the TDE black hole masses from MOSFiT, the KS test indicates the ANT population is different at $3\,\sigma$ significance.

Given that a significant number of the ANTs occurred in galaxies with likely non-negligible pre-existing accretion, we do not attempt to fit the host galaxy photometry to obtain a stellar mass to attempt to infer black hole masses.

5.1.4 Tidal disruption of dense gas cloud

The accretion of giant molecular clouds (GMCs) is a possible explanation to both ANTs as well as the rapid accretion rates necessary for the observed presence of very massive SMBHs at high redshift (e.g. Lin, Chen & Hwang 2023). The (partial) disruption and accretion of a GMC was suggested as an explanation for ZTF20abrbeie/AT2021lwx (Wiseman et al. 2023). However, GMCs near the Milky Way Galactic centre have radii of several pc and masses 10^4–$10^5\,\mathrm{M}_\odot$ (Miyazaki & Tsuboi 2000) so that such events are predicted to have durations of 10^4–10^5 yr for a $10^6\,\mathrm{M}_\odot$ SMBH

(Alig et al. 2011, 2013), and even longer for the more massive cases. Nevertheless, the near-ubiquitous MIR flares in our sample are strong evidence that dust and molecular gas is present at ~ 0.1–1 pc from the black hole. On these scales, the clouds are smaller (Hsieh et al. 2021), and around AGN, it is known that the cold and warm dust and molecular gas constituting the torus is clumpy (Krolik & Begelman 1988) and turbulent (Wada, Papadopoulos & Spaans 2009; Hoenig 2013, e.g) with many cloud–cloud collisions (e.g. Beckert & Duschl 2004). A scenario could thus be imagined where such a cloud–cloud collision results in a direct encounter between a small, dense cloud and the SMBH, resulting in super-Eddington accretion and an ANT-like flare.

5.2 Volumetric rate of ANTs

The intrinsic rate of transient events provides constraints on the physical mechanisms and plausible scenarios causing them. For example, for ANTs to be caused by high stellar mass TDEs, the rates should agree with the expected population of high-mass stars in SMBH loss cones. Such rate measurements are important for the inclusion of ANTs in simulations of galaxies and their nuclei, the understanding of stellar dynamics and black hole mass distributions (e.g. Stone & Metzger 2016) as well as for explaining the chemical abundances of AGN (e.g. Kochanek 2016). We estimate the volumetric rate of ANTs by using the seven events in the analysis sample that were selected by our pipeline. We limit the calculation to $z < 1$, the highest redshift event (ZTF20abrbeie/AT2021lwx). For each event, we calculate the maximum redshift that it would have passed our cuts, using the black body properties from Table 4. Using that maximum redshift, we then weight each transient by the maximum observable volume, $1/V_{\rm max}$ (Schmidt 1968). We assume the sky area of the public survey to be 15 000 deg^2 (Ho et al. 2023), and the survey time to be 4.77 yr (we cut the selection at 31/12/2023/MJD 60 309 so for the transient to last 1 yr, it must be first detected by MJD 59943). Counting the seven events in this manner, we estimate a lower limit on the rate $\gtrsim 5 \times 10^{-11}$ Mpc^{-1} yr^{-1}. Removing ZTF20aaqtncr/AT2021fez, which we classified as Unclear, gives a rate of $\gtrsim 3 \times 10^{-11}$ Mpc^{-1} yr^{-1}. We note that these measurements are ~ 50 times greater than those for 'extreme' ANTs (ENTs) measured by Hinkle et al. (2024), a sample of three with which we share one common event (ZTF20abrbeie/AT2021lwx). These rates are consistent with a direct extrapolation of the measured TDE luminosity function (i.e. rate per unit peak luminosity) in ZTF measured by Yao et al. (2023a). However, above the Hills mass of $M_{\rm BH} \geq 10^8$ M$_\odot$ for a solar mass star, the TDE rate should be heavily suppressed (e.g. Stone et al. 2020), and indeed such a suppression is observed (Mockler et al. 2019; Velzen et al. 2019; Nicholl et al. 2022). Wiseman et al. (2023) estimated that the rate of TDEs from ~ 15 M$_\odot$ stars should be 10^{-6} that of solar mass stars based on the slope of the initial mass function (IMF) and the lifetime of massive stars. Applying this fraction to the observed volumetric TDE rate of 3.1×10^{-7} Mpc^{-1} yr^{-1} (Yao et al. 2023a), we might expect $\sim 10^{-13}$ Mpc^{-1} yr^{-1} from ~ 15 M$_\odot$ stars. The TDE model fits to our ANT light curves returned stellar masses between 0.12–90 M$_\odot$, with seven in the range 1.5–10 M$_\odot$. Based upon the arguments of lifetimes and the IMF would expect significantly more TDEs from stars in this mass range than ~ 15 M$_\odot$. The observed rate $\gtrsim 3 \times 10^{-11}$ Mpc^{-1} yr^{-1} is thus consistent with the expectation for TDEs of stars in the 1.5–10 M$_\odot$ mass range. The increased depth of the Vera C. Rubin Observatory's Legacy Survey of Space and Time (LSST; Ivezic et al. 2019) will enhance the rate of observed TDEs Bučar Bricman et al. (2023) while hundreds will be spectroscopically classified by the Time Domain Extragalactic Survey (TiDES; Frohmaier et al. 2025) on the 4-metre Multi-Object Spectrograph Telescope. These observations will allow a detailed measurement of the rate of massive-star TDEs and ANTs.

5.3 Uniqueness of AT2021lwx

Despite a thorough search, no events were found with observed properties that are comparable properties to AT2021lwx. First, every event discovered using the linear fit was found with a clear host galaxy, with AT2021lwx itself the only hostless event passing the cuts. No other event in our sample has a luminosity as low as the limit of $M_r > -21$ mag for the host of AT2021lwx. Assuming a black body SED for the transient, two events (ZTF19aamrjar and ZTF20abodaps/AT2020afep) from the analysis sample come within ~ 0.3 dex of the peak UV-optical pesudo-bologmetric luminosity of AT2021lwx ($\log(L_{\rm bol,max}/{\rm erg\,s^{-1}}) = 45.85$). The light curve of ZTF19aamrjar is the most similar to AT2021lwx, and since it evolves much more slowly, the integrated energy release is larger than AT2021lwx. The spectrum is however vastly different: the Balmer line profiles are broad and asymmetric, and there is strong narrow oxygen. ZTF20abodaps/AT2020afep has a similar spectrum with no oxygen present. However, the sharp rise time is inconsistent with AT2021lwx.

6 CONCLUSIONS

In this paper, we have presented a systematically selected sample of ambiguous nuclear transients with smooth, slowly evolving optical light curves. The events appear to span the continuum between Bowen fluorescence flares and the extreme end of AGN variability. A summary of the key findings is below:

(i) We find eight nuclear events with long-duration (> 300 d), smooth, luminous ($L_{\rm BB} > 10^{44.7}$ erg s^{-1}) light curves similar to ZTF20abrbeie/AT2021lwx including ZTF20abrbeie/AT2021lwx itself.
(ii) We find three additional transients with bumpier light curves whose spectra do not resemble regular AGN or SNe.
(iii) The light curve properties are heterogeneous with rise times ranging from 20 d to 1 yr.
(iv) The spectra are also heterogeneous, ranging from quasar-like (ZTF19aamrjar), through NLSy1-like (ZTF18aczpgwm/AT2019kn) through to Balmer emission only (ZTF20abodaps/AT2020afep and ZTF20abrbeie/AT2021lwx).
(v) Mid-infrared flares are near ubiquitous, implying the presence of circumnuclear dust.
(vi) Modelling the light curves as TDEs, the inferred black hole masses and stellar masses are beyond the ranges observed for canonical TDEs. The volumetric rate of $\gtrsim 3 \times 10^{-11}$ Mpc^{-1} yr^{-1} is consistent with rough predictions of disruptions of intermediate high-mass stars.
(vii) ANTs have rise times longer than and amplitudes greater than regular AGN variability. We define a region of rise-time versus flare amplitude parameter space for a complete selection of ANTs that is ~ 50 per cent contaminated by AGN.

If these ANTs, along with those compiled from other surveys, are indeed TDEs, then the emission mechanism for the bulk of the radiation must be different to the canonical TDE of a 1 M$_\odot$ star around a 10^5–10^7 M$_\odot$ black hole in order to produce the markedly different optical spectra.

We expect to observe > 100 AT2021lwx-like ANTs with LSST and will be able to statistically model their light curve, spectral, and host galaxy properties.

ACKNOWLEDGEMENTS

We thank the referee for their thoughtful comments which have greatly improved the work. We thank Karri Koljonen for providing the spectra and reduced UVOT data for ZTF22aadesap/AT2022fpx. We thank S. Smartt and the Pan-STARRS team for providing data points of ZTF19aamrjar, ZTF20abodaps, ZTF18aczpgwm, ZTF19aatubsj, and ZTF20aanxcpf to support the figures in the appendix. We are grateful to Matt Stepney and Daniel Kynoch for their advice and insights on AGN spectra and Sandra Raimundo for discussions about CLAGNs.

PW acknowledges support from the Science and Technology Facilities Council (STFC) grant ST/R000506/1. IA acknowledges support from the European Research Council (ERC) under the European Union's Horizon 2020 research and innovation program (grant agreement number 852097), from the Israel Science Foundation (grant number 2752/19), from the United States–Israel Binational Science Foundation (BSF; grant number 2018166), and from the Pazy Foundation (grant no. 216312). LG acknowledges financial support from the Spanish Ministerio de Ciencia e Innovación (MCIN), the Agencia Estatal de Investigación (AEI) 10.13039/501100011033, the European Social Fund (ESF) 'Investing in your future', the European Union Next Generation EU/PRTR funds under the PID2020-115253GA-I00 HOSTFLOWS project, the 2019 Ramón y Cajal programme RYC2019-027683I, the 2021 Juan de la Cierva programme FJC2021-047124-I, Centro Superior de Investigaciones Científicas (CSIC) under the PIE project 20215AT016, and the program Unidad de Excelencia María de Maeztu CEX2020-001058-M. MN was supported by the European Research Council (ERC) under the European Union's Horizon 2020 research and innovation programme (grant agreement no. 948381) and by UK Space Agency grant no. ST/Y000692/1. TP acknowledges the financial support from the Slovenian Research Agency (grant P1-0031). DI acknowledges funding provided by the University of Belgrade–Faculty of Mathematics (the contract no. 451-03-66/2024-03/200104) through the grant of the Ministry of Science, Technological Development and Innovation of the Republic of Serbia. MJG acknowledges support from the National Science Foundation (grant AST-2108402).

Lasair is supported by the UKRI Science and Technology Facilities Council and is a collaboration between the University of Edinburgh (grant ST/N002512/1) and Queen's University Belfast (grant ST/N002520/1) within the LSST:UK Science Consortium.

DATA AVAILABILITY

All of the ZTF light curves from Lasair are freely available, for example https://lasair-ztf.lsst.ac.uk/object/ZTF19aamrjar, and others following the same pattern.

All photometric and spectroscopic data presented in this manuscript are available at https://github.com/wisemanp/ANTs-Nest.

REFERENCES

Abdurro'uf et al., 2022, ApJS, 259, 35
Alig C., Burkert A., Johansson P. H., Schartmann M., 2011, MNRAS, 412, 469
Alig C., Schartmann M., Burkert A., Dolag K., 2013, ApJ, 771, 119
Ambikasaran S., Foreman-Mackey D., Greengard L., Hogg D. W., O'Neil M., 2015, IEEE Trans. Pattern Anal. Mach. Intell., 38, 252
Andreoni I. et al., 2022, Nature, 612, 430
Angus C. R. et al., 2019, MNRAS, 487, 2215
Antonucci R., 2018, Nat. Astron., 2, 504
Arcavi I. et al., 2014, ApJ, 793, 38
Baldwin J. A., Phillips M. M., Terlevich R., 1981, PASP, 93, 5
Bauer A., Baltay C., Coppi P., Ellman N., Jerke J., Rabinowitz D., Scalzo R., 2009, ApJ, 696, 1241
Beckert T., Duschl W. J., 2004, A&A, 426, 445
Bellm E. C. et al., 2019, PASP, 131, 018002
Blagorodnova N. et al., 2017, ApJ, 844, 46
Blanchard P. K. et al., 2017, ApJ, 843, 106
Brennan S., Fraser M., Ihanec N., Gromadzki M., Yaron O., 2019, Transient Name Server Classification Report, 2019-1595, 1
Brown T. M. et al., 2013, PASP, 125, 1031
Bučar Bricman K., van Velzen S., Nicholl M., Gomboc A., 2023, ApJS, 268, 13
Burrows D. N. et al., 2005, Space Sci. Rev., 120, 165
Buzzoni B. et al., 1984, The Messenger, 38, 9
Cannizzaro G. et al., 2020, MNRAS, 493, 477
Caplar N., Lilly S. J., Trakhtenbrot B., 2017, ApJ, 834, 111
Cepa J. et al., 2000, in Masanori I., Moorwood A. F., eds, Proc. SPIE Conf. Ser. Vol. 4008, Optical and IR Telescope Instrumentation and Detectors. SPIE, Bellingham, p. 623
Chambers K. C. et al., 2016, preprint (arXiv:1612.05560)
Chan C.-H., Piran T., Krolik J. H., Saban D., 2019, ApJ, 881, 113
Charalampopoulos P. et al., 2022, A&A, 659, A34
Chen Z. H. et al., 2023, ApJ, 943, 41
Chornock R., Blanchard P. K., Gomez S., Hosseinzadeh G., Berger E., 2019, Transient Name Server Classification Report, 2019-1016, 1
Chu M., Dahiwale A., Fremling C., 2021a, Transient Name Server Classification Report, 2021-2580, 1
Chu M., Dahiwale A., Fremling C., 2021b, Transient Name Server Classification Report, 2021-3495, 1
Clavel J. et al., 1992, ApJ, 393, 113
De Cicco D. et al., 2022, A&A, 664, A117
Dgany Y., Arcavi I., Makrygianni L., Pellegrino C., Howell D. A., 2023, ApJ, 957, 57
Dong S. et al., 2016, Sci, 351, 257
Drout M. R. et al., 2014, ApJ, 794, 23
Eracleous M., Boroson T. A., Halpern J. P., Liu J., 2012, ApJS, 201, 23
Fitzpatrick E. L., 1999, PASP, 111, 63
Frederick S. et al., 2021, ApJ, 920, 56
Frohmaier C. et al., 2025, MNRAS, preprint (arXiv:2501.16311)
Gehrels N. et al., 2004, ApJ, 611, 1005
Gezari S., 2021, ARA&A, 59, 21
Graham M. J. et al., 2019, PASP, 131, 078001
Graham M. J., Djorgovski S. G., Drake A. J., Stern D., Mahabal A. A., Glikman E., Larson S., Christensen E., 2017, MNRAS, 470, 4112
Grayling M. et al., 2022, TNSAN, 195, 1
Guillochon J., Nicholl M., Villar V. A., Mockler B., Narayan G., Mandel K. S., Berger E., Williams P. K. G., 2018, ApJS, 236, 6
Hammerstein E. et al., 2021, Transient Name Server Classification Report, 2021-955, 1
Hammerstein E. et al., 2023, ApJ, 942, 9
Hills J. G., 1975, Nature 1975 254:5498, 254, 295
Hinkle J. T. et al., 2024, Science, preprint (arXiv:2405.08855)
Hinkle J. T., 2024, MNRAS, 531, 2603
Ho A. Y. Q. et al., 2023, ApJ, 949, 120
Hodgkin S. T. et al., 2021, A&A, 652, A76
Hoenig S. F., 2013, preprint (arXiv:1301.1349)
Holoien T. W.-S. et al., 2022, ApJ, 933, 196
Hsieh P.-Y. et al., 2021, ApJ, 913, 94
Hughes P. A., Aller H. D., Aller M. F., 1992, ApJ, 396, 469
Inserra C., Prajs S., Gutierrez C. P., Angus C., Smith M., Sullivan M., 2018, ApJ, 854, 175
Ivezic Z. et al., 2019, ApJ, 873, 111

Jiang N. et al., 2021a, ApJS, 252, 32
Jiang N., Wang T., Hu X., Sun L., Dou L., Xiao L., 2021b, ApJ, 911, 31
Kankare E. et al., 2017, Nat. Astron., 1, 865
Kauffmann G. et al., 2003, MNRAS, 341, 33
Kelly B. C., Bechtold J., Siemiginowska A., 2009, ApJ, 698, 895
Kewley L. J., Dopita M. A., Sutherland R. S., Heisler C. A., Trevena J., 2001, ApJ, 556, 121
Kochanek C. S., 2016, MNRAS, 458, 127
Koljonen K. I. I. et al., 2024, MNRAS, 532, 112
Kozłowski S., 2016, ApJ, 826, 118
Krolik J. H., Begelman M. C., 1988, ApJ, 329, 702
Krühler T., et al. 2018, A&A, 610, A14
Lacy M. et al., 2020, PASP, 132, 035001
LaMassa S. M. et al., 2015, ApJ, 800, 144
Lawrence A., 2018, Nat. Astron., 2, 102
Leloudas G. et al., 2016, Nat. Astron., 1, 0002
Leloudas G. et al., 2019, ApJ, 887, 218
Lin C.-H., Chen K.-J., Hwang C.-Y., 2023, ApJ, 952, 121
Lipunova G. V., Tavleev A. S., Malanchev K. L., 2024, A&A, preprint (arXiv:2404.08441)
MacLeod C. L. et al., 2010, ApJ, 721, 1014
MacLeod C. L. et al., 2016, MNRAS, 457, 389
Mainzer A. et al., 2011, ApJ, 731, 53
Makrygianni L. et al., 2023, ApJ, 953, 32
Masci F. et al., 2018, ATel, 11685, 1
Masci F. J. et al., 2019, PASP, 131, 018003
Masterson M. et al., 2024, ApJ, 961, 211
McHardy I. M. et al., 2016, Astron. Nachr., 337, 500
McKernan B., Ford K. E. S., Cantiello M., Graham M., Jermyn A. S., Leigh N. W. C., Ryu T., Stern D., 2022, MNRAS, 514, 4102
Merloni A. et al., 2015, MNRAS, 452, 69
Miyazaki A., Tsuboi M., 2000, ApJ, 536, 357
Mockler B., Guillochon J., Ramirez-Ruiz E., 2019, ApJ, 872, 151
Mor R., Netzer H., 2012, MNRAS, 420, 526
Mor R., Netzer H., Elitzur M., 2009, ApJ, 705, 298
Neustadt J. M. M. et al., 2020, MNRAS, 494, 2538
Newsome M. et al., 2024, ApJ, 977, 258
Nicholl M. et al., 2020, MNRAS, 499, 482
Nicholl M., 2018, Res. Notes AAS, 2, 230
Nicholl M., Lanning D., Ramsden P., Mockler B., Lawrence A., Short P., Ridley E. J., 2022, MNRAS, 515, 5604
Nicholl M., Williams P. K. G., Berger E., Villar V. A., Alexander K. D., Eftekhari T., Metzger B. D., 2017, ApJ, 843, 84
Oates S. R. et al., 2024, MNRAS, 530, 1688
Oke J. B., Gunn J. E., 1983, ApJ, 266, 713
Oke J. et al., 1995, PASP, 107, 375
Osterbrock D. E., 1989, Astrophysics of Gaseous Nebulae and Active Galactic Nuclei. University Science Books
Pellegrino C., Li W., Burke J., Howell D. A., McCully C., Newsome M., Gonzalez E. P., Terreran G., 2022, Transient Name Server Classification Report, 2022-1677, 1
Perez-Fournon I. et al., 2022, Transient Name Server Classification Report, 2022-1771, 1
Perley D. A., 2019, PASP, 131, 084503
Petrushevska T. et al., 2023, A&A, 669, A140
Pitik T., Tamborra I., Angus C. R., Auchettl K., 2022, ApJ, 929, 163
Prasad C., Wang Y., Perna R., Ford K. E. S., McKernan B., 2024, MNRAS, 531, 1409
Predehl P. et al., 2021, A&A, 647, A1
Prochaska J. X. et al., 2020a, pypeit/PypeIt: Release 1.0.0 (v1.0.0). Zenodo. Available at: https://doi.org/10.5281/zenodo.3743493
Prochaska J. X. et al., 2020b, J. Open Source Softw., 5, 2308
Pursiainen M. et al., 2018, MNRAS, 481, 894
Pursiainen M. et al., 2020, MNRAS, 494, 5576
Quimby R. M. et al., 2011, Nature, 474, 487
Rasmussen C. E., Williams C. K. I., 2005, Gaussian Processes for Machine Learning. The MIT Press, Cambridge, MA
Rees M. J., 1988, Nature, 333, 523
Reusch S. et al., 2022, Phys. Rev. Lett., 128, 221101
Ricci C., Trakhtenbrot B., 2023, Nat. Astron, 7, 1282
Richards G. T. et al., 2002, AJ, 123, 2945
Ridley E. J. et al., 2024, MNRAS, 531, 1905
Roming P. W. A. et al., 2005, Space Sci. Rev., 120, 95
Rumbaugh N. et al., 2018, ApJ, 854, 160
Schlafly E. F., Finkbeiner D. P., 2011, ApJ, 737, 103
Schmidt M., 1968, ApJ, 151, 393
Shapovalova A. I. et al., 2016, ApJS, 222, 25
Sheng X., Ross N., Nicholl M., 2022, MNRAS, 512, 5580
Shingles L. et al., 2021, Transient Name Server AstroNote, 7, 1
Smartt S. J. et al., 2015, A&A, 579, A40
Smartt S. J. et al., 2024, MNRAS, 528, 2299
Smith K. W. et al., 2019, Res. Notes Am. Astron. Soc., 3, 26
Smith K. W. et al., 2020, PASP, 132, 1
Sniegowska M., Czerny B., Bon E., Bon N., 2020, A&A, 641, A167
Stone N. C., Metzger B. D., 2016, MNRAS, 455, 859
Stone N. C., Vasiliev E., Kesden M., Rossi E. M., Perets H. B., Amaro-Seoane P., 2020, Space Sci. Rev., 216, 35
Subrayan B. M. et al., 2023, ApJ, 948, L19
Sunyaev R. et al., 2021, A&A, 656, A132
Tachibana Y., Miller A. A., 2018, PASP, 130, 128001
Terreran G. et al., 2020, Transient Name Server Classification Report, 2020-2617, 1
Tonry J. L. et al., 2018, PASP, 130, 064505
Trakhtenbrot B. et al., 2019a, Nat. Astron., 3, 242
Trakhtenbrot B. et al., 2019b, ApJ, 883, 94
Valenti S. et al., 2014, MNRAS, 438, L101
van Velzen S. et al., 2018, Astron. Telegram, 12263, 1
van Velzen S. et al., 2021, ApJ, 908, 4
van Velzen S., Mendez A. J., Krolik J. H., Gorjian V., 2016, ApJ, 829, 19
van Velzen S., Stone N. C., Metzger B. D., Gezari S., Brown T. M., Fruchter A. S., 2019, ApJ, 878, 82
Vanden Berk D. E. et al., 2001, AJ, 122, 549
Vanden Berk D. E. et al., 2004, ApJ, 601, 692
Wada K., Papadopoulos P. P., Spaans M., 2009, ApJ, 702, 63
Wainscoat R., Chambers K., Lilly E., Weryk R., Chastel S., Denneau L., Micheli M., 2016, IAU Symp., Vol. 318, Asteroids: New Observations, New Models. Cambridge Univ. Press, Cambridge, p. 293
Wang Y. et al., 2022, ApJS, 258, 21
Wiseman P. et al., 2020, MNRAS, 498, 2575
Wiseman P. et al., 2023, MNRAS, 522, 3992
Yao Y. et al., 2023a, ApJ, 955, L6
Yao Y., Qin Y., Guolo M., 2023b, Transient Name Server Classification Report, 2023-962, 1
Yaron O., Gal-Yam A., 2012, PASP, 124, 668
York D. G. et al., 2000, AJ, 120, 1579

APPENDIX A: VARYING SELECTION CRITERIA

Here, we test our selection criteria with three variations on the nominal 'gold' selection described in Section 2.2.

A1 Decline time longer than rise time

The first variation is to impose a requirement that the decline time is longer than the rise time, as expected for accretion-powered transients. 21 transients pass this cut, which we label the 'platinum' selection.

A2 Faster light curves

The second variation is to relax the light curve duration to $\geq$ 0.5 yr. We also relax the number of detections to 25. This allows for faster-evolving events, and events with limited visibility

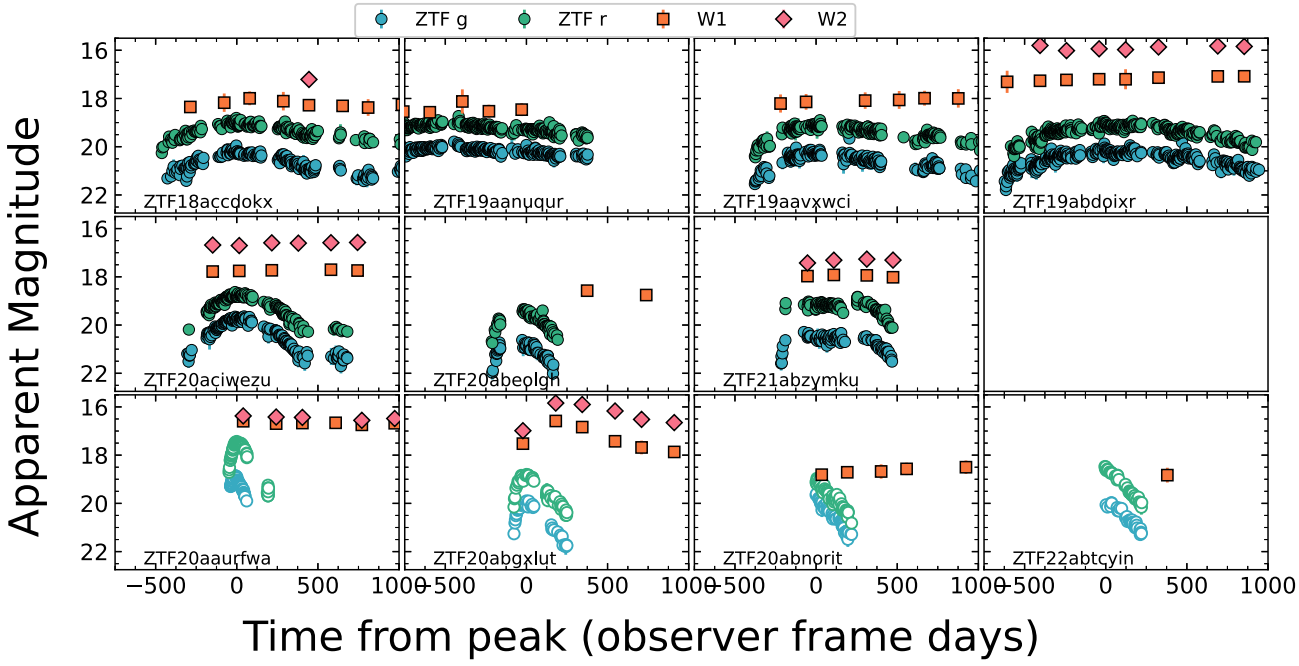

Figure A1. Optical and MIR light curves of the 7 ANTs passing 'bumpier' cuts (filled circles) and the 4 passing 'faster' cuts (open circles).

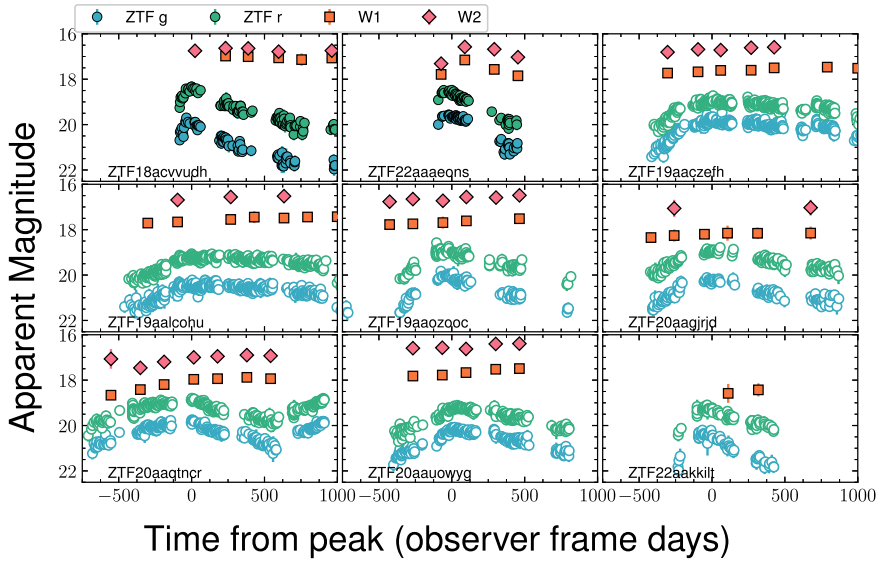

Figure A2. Optical and MIR light curves of the 2 ANTs passing 'gold' cuts but without spectroscopic redshift (filled circles) and the 4 passing gold cuts but in known QSOs (open circles).

(e.g. a 150 d rise was unobservable from Palomar but a subsequent 200 d decline was observed). It also means the contamination from regular transients is increased. 95 transients pass this 'faster' selection, of which 11 pass visual inspection having not already been included in the gold sample. Of the 11, there are three spectroscopically classified SNe IIn: ZTF19abpvbzf appears in a knot of star formation in an irregular galaxy, ZTF22aadesjc appears visually off-centre in a dwarf galaxy, but ZTF22aaurfwa=SN2022hem is only classified by a low-resolution spectrum and may be an ANT although the post-peak colour evolution is more consistent with the SN II classification. Four objects are spectroscopically classified TDEs: ZTF18abxftqm = AT2018hco (Velzen et al. 2018), ZTF20abnorit = AT2020ysg (Hammerstein et al. 2023), ZTF20achpcvt = AT2020vwl (Hammerstein et al. 2021). ZTF23aadcbay = AT2023cvb (Yao, Qin & Guolo 2023b). ZTF18aaqkcso is a type Ia SN. In Fig. A1, we show the light curve of ZTF20aaurfwa/SN2022hem, along with ZTF20abnorit/AT2020ysg which is classified as TDE-featureless and thus is ambiguous.

A3 Bumpier light curves

The third variation is to relax the constraint on the linear fit to $R^2 \geq 0.5$, allowing for noisier and/or bumpier light curves. 550 events pass these criteria, many of which are regular AGN-like variability. 10 of these events are labelled ANTs in visual inspection. Of these 10, three are known QSOs while one (ZTF20acklcyp) is spectroscopically

classified as a SN IIn (SN2020xkx). The remaining six are shown in Fig. A1.

A4 ANTs with no spectra

ZTF18acvvudh and ZTF22aaaeons passed our gold (and platinum) selection cuts and visual inspection, but do not have spectra or redshifts and thus are not included in the main analysis. Their light curves are shown in filled circles in Fig. A2.

A5 ANTs in known QSOs

Four events, ZTD19aaczefh, ZTF19aalcohu, ZTF20aagjrjd, and ZTF22aakkilt, show ANT-like light curves but occurred in known spectroscopic quasi-stellar objects (QSOs, i.e. high-z AGNs). In contrast to our analysis sample, they show minimal MIR evolution.

APPENDIX B: FULL LIGHT CURVES

In Figs B1, B2, B3, B4, B5, B6, B7, B8, B9, B10, B11 we present all the available photometric data for each ANT in our main sample.

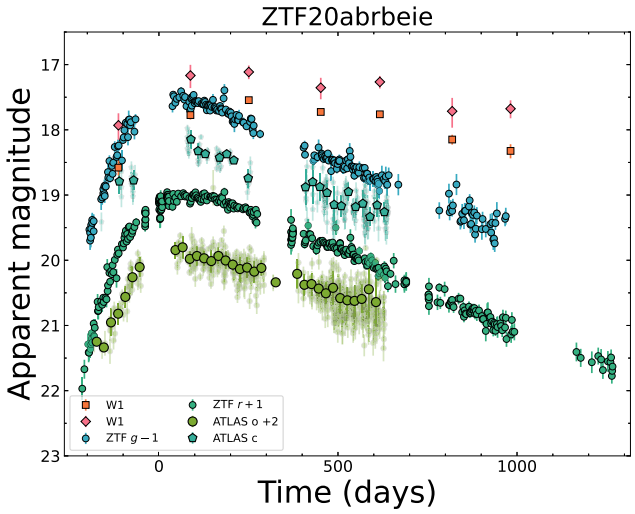

Figure B1. Observer frame light curve of ZTF20abrbeie relative to r-band maximum light.

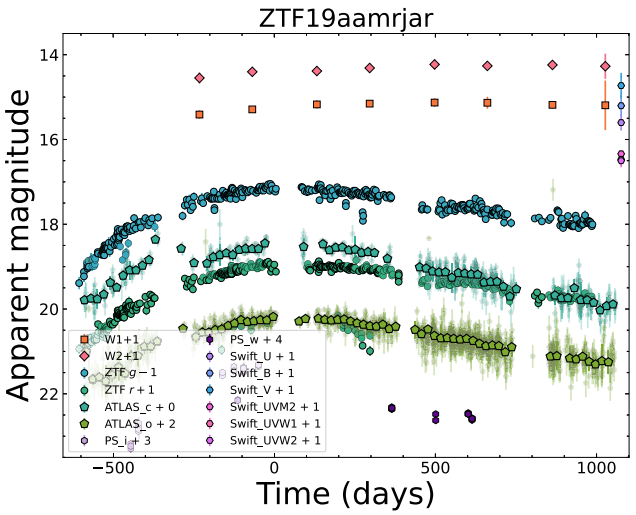

Figure B2. Observer frame light curve of ZTF19aamrjar relative to r-band maximum light.

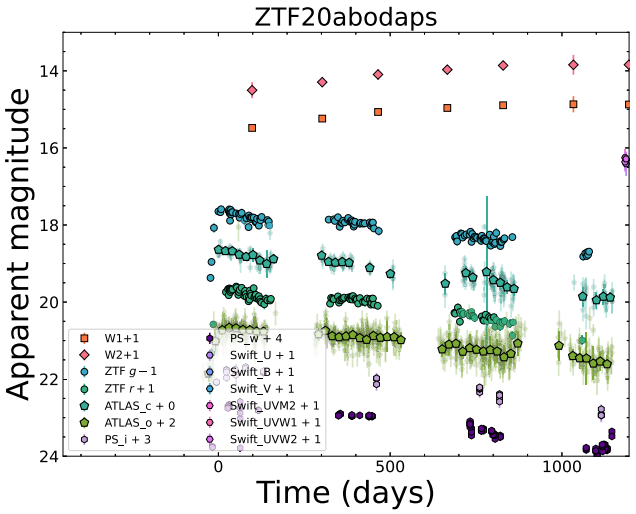

Figure B3. Observer frame light curve of ZTF20abodaps relative to r-band maximum light.

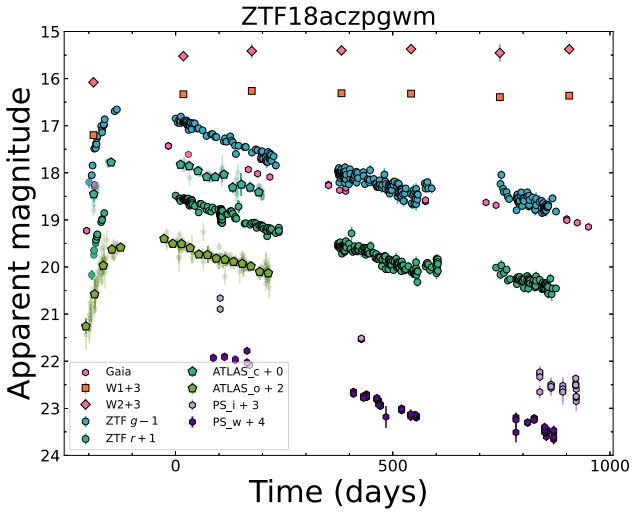

Figure B4. Observer frame light curve of ZTF18aczpgwm relative to r-band maximum light.

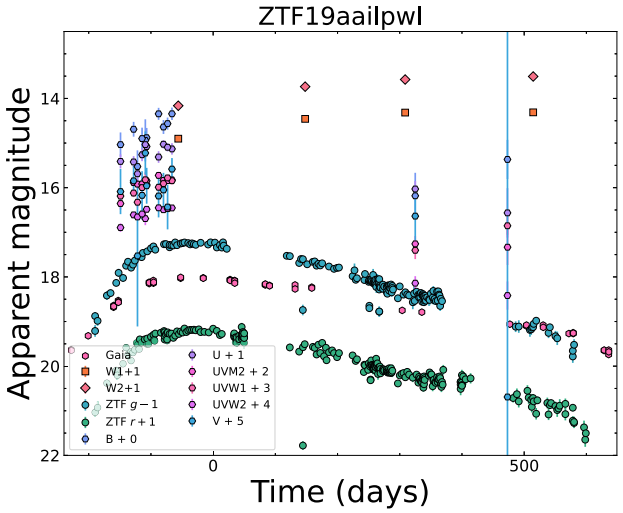

Figure B6. Observer frame light curve of ZTF19aailpwl relative to r-band maximum light.

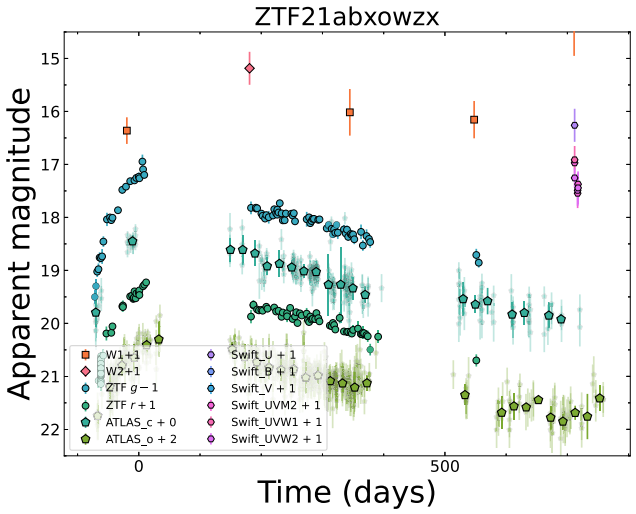

Figure B5. Observer frame light curve of ZTF21abxowzx relative to r-band maximum light.

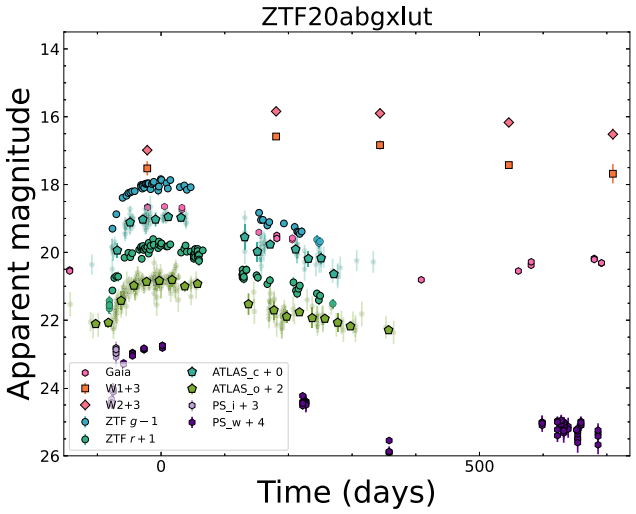

Figure B7. Observer frame light curve of ZTF20abgxlut relative to r-band maximum light.

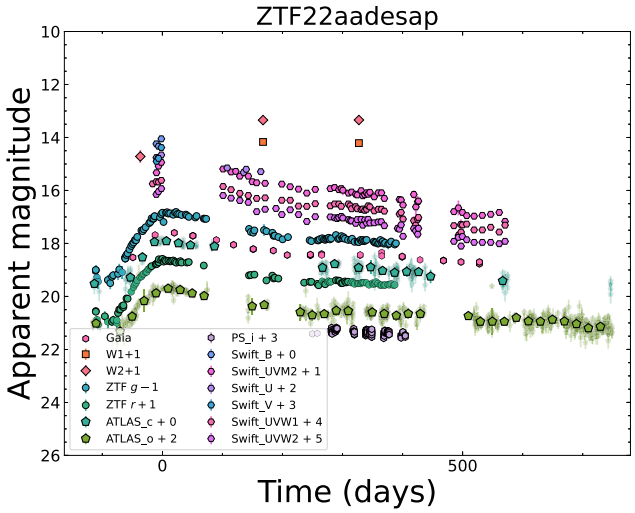

Figure B8. Observer frame light curve of ZTF22aadesap relative to r-band maximum light

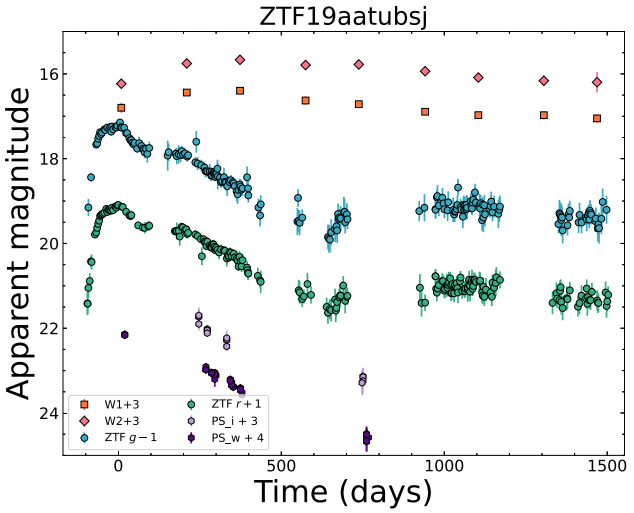

Figure B10. Observer frame light curve of ZTF19aatubsj relative to r-band maximum light.

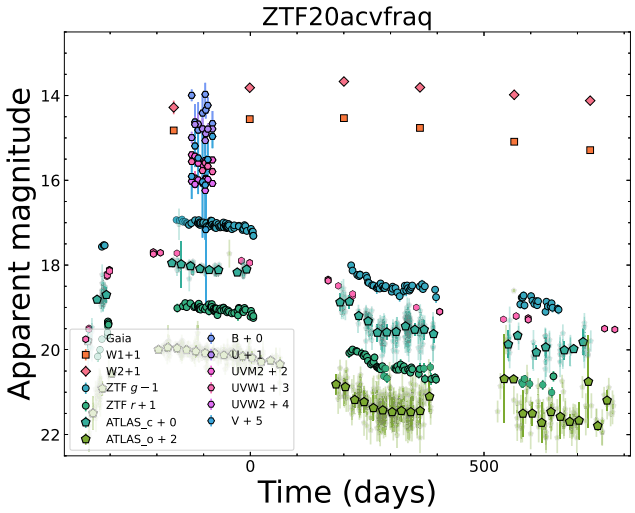

Figure B9. Observer frame light curve of ZTF20acvfraq relative to r-band maximum light.

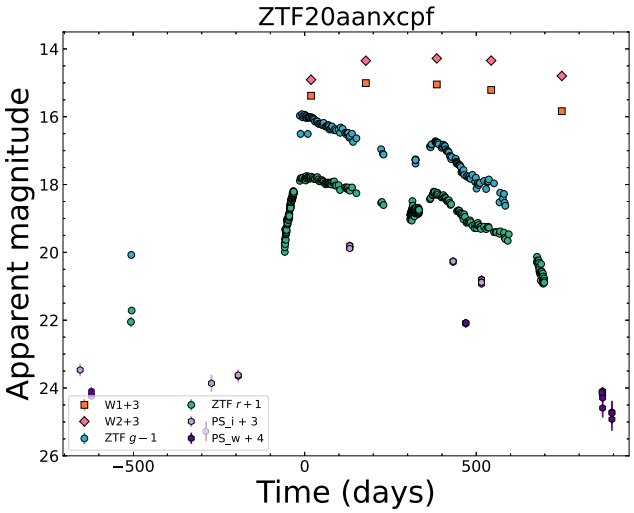

Figure B11. Observer frame light curve of ZTF20aanxcpf relative to r-band maximum light.

This paper has been typeset from a TEX/LATEX file prepared by the author.